ADVANCING EARTH AND SPACE SCIENCE

JGR Solid Earth

RESEARCH ARTICLE
10.1029/2022JB025678

Laboratory Investigation of Hydraulic Fracture Growth in Zimbabwe Gabbro

Dong Liu[1] **and Brice Lecampion**[1]

[1]Geo-Energy Laboratory—Gaznat Chair on Geo-Energy, EPFL-ENAC-IIC-GEL, Station 18, École Polytechnique Fédérale de Lausanne (EPFL), Lausanne, Switzerland

Key Points:

- Hydraulic fractures exhibit higher apparent macroscopic toughness during propagation compared to semicircular bending tests
- Fracture bridges and segments are observed at the millimeter scale, while the geometry remains circular and planar at the centimeter scale
- The presence of fracture segments and their coalescence is likely responsible for the higher apparent fracture energy at macroscopic scale

Supporting Information:

Supporting Information may be found in the online version of this article.

Correspondence to:

B. Lecampion,
brice.lecampion@epfl.ch

Citation:

Liu, D., & Lecampion, B. (2022). Laboratory investigation of hydraulic fracture growth in Zimbabwe gabbro. *Journal of Geophysical Research: Solid Earth*, *127*, e2022JB025678. https://doi.org/10.1029/2022JB025678

Received 23 SEP 2022
Accepted 25 OCT 2022

Author Contributions:

Conceptualization: Dong Liu, Brice Lecampion
Data curation: Dong Liu
Formal analysis: Dong Liu, Brice Lecampion
Funding acquisition: Brice Lecampion
Investigation: Dong Liu
Methodology: Dong Liu, Brice Lecampion
Supervision: Brice Lecampion
Visualization: Dong Liu
Writing – original draft: Dong Liu
Writing – review & editing: Brice Lecampion

Abstract Direct measurement of the apparent toughness evolution during hydraulic fracture growth remains challenging in rocks due to the difficulty of measuring the time evolution of the fracture geometry. We report hydraulic fracturing tests performed in 250 × 250 × 250 mm Zimbabwe gabbro under different confining stress. Using time-lapse active acoustic surveys, we reconstruct the fracture front and fracture width using scattered and transmitted waves. After verifying that hydraulic fracture growth is dominated by the energy dissipated in fracture creation such that the fluid pressure can be considered spatially uniform in the fracture (negligible viscous flow energy dissipation), we estimate the apparent fracture toughness, using the theory of linear hydraulic fracture mechanics, by combining fracture geometry and pressure data. The apparent fracture energy is higher than that measured from semicircular bending tests. The created fractures evolve in a planar and radial geometry at the macroscopic scale, but we observe overlapping segments and bridges at the millimetric scale. This complex segmentation at a scale on par with the rock grain size is likely responsible for the observed higher fracture energy at centimetric scale. Such fracture segmentation and bridging will necessarily occur when encountering heterogeneities and result in a further increase of fracture energy at a larger scale even if the overall macroscopic geometry remains planar. The experimental data set reported here should guide modeling efforts necessary to better predict hydraulic fracture growth in rock masses.

Plain Language Summary Well completion for fluids extraction or injection at depth often requires hydraulic stimulation to achieve economical fluid flow rates. Predicting the growth of fluid-driven fractures in geological systems is essential for the sustainable and efficient engineering of porous reservoirs. The linear hydraulic fracture mechanics (LHFM) which combines linear elastic fracture mechanics and lubrication flow has proven to accurately describe fracture growth in brittle materials. However, deviations from LHFM predictions, such as a larger pressure and a shorter fracture length, are reported for hydraulic fracture injections in rocks, which implies a larger energy dissipation. We report the evolution of the fracture geometry, pressure, and estimates of the apparent energy during propagation of hydraulic fracture in rocks under laboratory conditions. The fractures are planar and evolve in a radial way at the centimeter scale, but consist of multiple overlapping segments at the millimeter scale. This fracture morphology induced by local heterogeneities influences the hydromechanical coupling during hydraulic fracture growth, and results in larger energy dissipation.

1. Introduction

Linear elastic fracture mechanics (LEFM) combined with lubrication theory (linear hydraulic fracture mechanics—LHFM for short) have successfully predicted hydraulic fracture growth for planar geometry in model materials such as Poly(methyl methacrylate) (PMMA) and glass (Bunger & Detournay, 2008; Lecampion et al., 2017; Wu et al., 2008; Xing et al., 2016). However, deviations from LHFM predictions, such as a larger fluid pressure, have been reported in laboratory experiments in rocks (Makhnenko et al., 2010; Thallak et al., 1993; van Dam & de Pater, 1999) as well as microhydraulic fracture tests in deep wellbores (Shlyapobersky, 1985; Shlyapobersky et al., 1988). These deviations have been attributed to the presence of a nonnegligible fracture process zone around the fracture tip where progressive distributed microcracking or other damage takes place (Bao & Suo, 1992; Bažant, 1984; Kinloch & Williams, 1980; Labuz et al., 1987; Steinhardt & Rubinstein, 2022; Tvergaard & Hutchinson, 1992). When the process zone is large compared to the fracture or other characteristic dimensions of the samples, LEFM fails to capture the stress field near the fracture tip or predict the fracture growth (Bažant, 1984; Bazant & Planas, 1998). In addition, fluid flow inside the process zone likely deviates from lubrication theory and further enhances the nonlinear hydromechanical coupling at play (Liu & Lecampion, 2021). Accounting for the

Table 1
Zimbabwe Gabbro Properties

Bulk density ρ ($\times 10^3$ kg/m^3)	Porosity (%)	Grain size (mm)	E (GPa)	ν (·)	K_{Ic} (MPa · m$^{1/2}$)
3.00	0.32	1–3	99.7	0.29	2.79 ± 0.11

Note. The elastic properties have been measured via quasi-static triaxial tests (Vásquez et al., 2022) at a confinement of 0 and 10 MPa (with similar values for both confinement), and the mode I fracture toughness from semicircular bending (SCB) test (Kuruppu et al., 2014). The connected pore volume was measured by gas pycnometer.

nonlinear process zone during the hydraulic fracture growth, theoretical predictions have reported an increase of fracture energy dissipation dependent on the confining stress (Garagash, 2019; Liu & Lecampion, 2019a, 2019b, 2021; Papanastasiou, 1999). However, few studies have reported the time evolution of apparent fracture energy for hydraulic fracture propagation in rocks.

Hydraulic fracturing is a volumetric controlled process characterized by negligible inertia. It is essentially a quasi-static process (Detournay, 2016). As a result, the apparent fracture toughness can be estimated from the mode I stress intensity factor in fracture mechanics (Rummel, 1987). Estimation of the stress intensity factor requires the measurement of (a) the evolution of fracture dimensions during propagation and (b) the fluid pressure distribution inside the fracture. The fluid pressure can be only measured at the wellbore for most cases in the laboratory and field (Warpinski, 1985). It can be representative of the fluid pressure inside the fracture when viscous pressure drops (at the fracture entrance and within the fracture) become negligible. This can be achieved by adequately controlling the fluid viscosity and injection rate (Bunger & Detournay, 2008). The main difficulty for the estimation of fracture apparent energy thus resides in the proper measurement of fracture dimensions in rocks. Early attempts to measure the fracture geometry date back to the 1950s (Haimson, 1968; Hubbert & Willis, 1957) when only postmortem observations of the created fractures were reported in laboratory hydraulic fracture experiments. Advancement in imaging techniques (such as the observation of fracture thin sections using optical microscope (Chen et al., 2015; Lhomme, 2005), and 3D imaging of the fractured plane using CT scan (Renard et al., 2009)) during the last decades has improved a lot the description of the postmortem fracture geometry. However, the inspection of the evolution of hydraulic fracture dimensions with time mostly relies on acoustic monitoring methods. Compared with other inverted imaging techniques, such as neutron imaging (Roshankhah et al., 2018) and self-potential methods (Haas et al., 2013; Moore & Glaser, 2007), acoustic monitoring has been widely applied in the laboratory due to its good balance between measurement accuracy, sample size, and cost. One can obtain the development of rupture front through the localization of acoustic emission with passive acoustic listening (Lockner & Byerlee, 1977; Stanchits et al., 2014; Stoeckhert et al., 2015; Zoback et al., 1977). Such a technique is however insufficient for direct quantification of the fracture width and fracture extent, which further necessitates the usage of active acoustic monitoring by analyzing the changes of scattering and transmitted waves interacting with the growing fracture (Groenenboom & Fokkema, 1998; Groenenboom & van Dam, 2000; Liu et al., 2020; Medlin & Masse, 1984).

In this paper, we conduct hydraulic fracturing injections in cubic Zimbabwe gabbro samples with a dimension of 250 mm. Following the theories of LHFM (Detournay, 2016; Savitski & Detournay, 2002), we ensure that the fracture propagates in the so-called toughness dominated regime, where the energy is mostly dissipated by the creation of new fracture surfaces rather than viscous fluid flow. This leads to an approximately uniform pressure distribution inside the fracture such that wellbore pressure measurement can be used as representing the fracture pressure. We reconstruct the evolution of the fracture dimensions via the use of an unprecedented number of active acoustic transducers. Following the methods and techniques described in Liu et al. (2020), we relax the previous assumption of a strictly symmetric and centered fracture (Groenenboom & Fokkema, 1998; Medlin & Masse, 1984), in order to capture the spatiotemporal evolution of the fracture dimensions with higher accuracy. By estimating the apparent toughness via the fluid pressure and fracture dimensions, we aim to investigate how hydraulic fracture growth deviates from the LHFM predictions, and the possible mechanisms responsible for these deviations.

2. Materials and Methods

We investigate hydraulic fracture growth in Zimbabwe gabbro in the so-called toughness dominated regime where viscous flow dissipation is negligible (Detournay, 2016). Zimbabwe gabbro is a very low porosity/permeability rock which can be considered impermeable at the scale of the injection investigated here. Its main properties are listed in Table 1. The rock samples are cut and rectified into a 250 mm cubic sample. A wellbore of 16-mm diameter is drilled vertically through the block. As shown in Figure 1, a horizontal radial notch with a diameter of 21 ± 1 mm is created by rotating a T-shape notching tool with its stem part applied onto the wall of the wellbore. The distance between the bottom of the notching tool and the top surface of the sample is kept

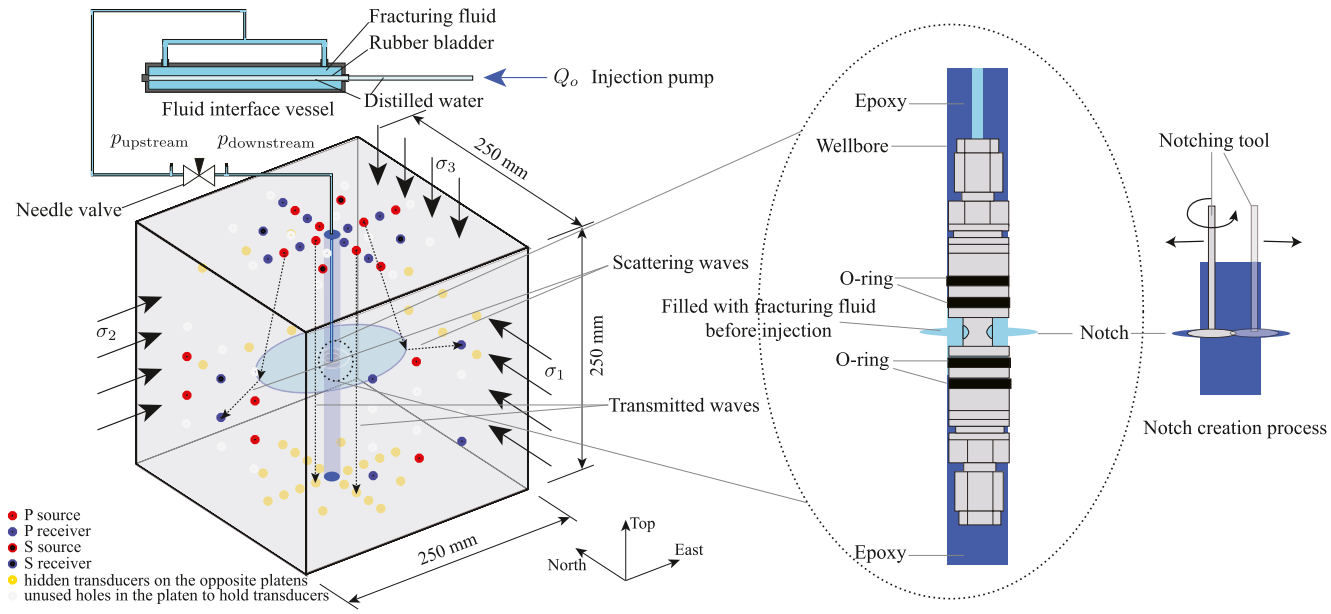

Figure 1. Schematic illustration of the experimental setup showing the transducers' disposition. Additional holes are available in the platens allowing the use of various transducer dispositions. Two facing platens share the same transducers disposition and source/receiver transducers are alternatively located on opposite platens for robustness.

constant so that the notch is created at the center of the sample to localize fracture initiation. A completion tool connected to an injection tubing is then glued in the wellbore with epoxy. This ensures an injection of the fluid only at the level of the notch.

The specimens are loaded in a true triaxial frame where the confinement is applied via symmetric pairs of flat jacks in the three different axis. Each flat jack pair is connected to a pressure-volume controller (GDS High-Pressure-Volume Controller, 200 mL) which controls the compressive stresses applied on each axis with a maximum of 20 MPa. The confinement is set prior to the start of injection and is kept constant throughout the experiment via the pressure-volume controller. The volume and pressure evolution of the three pressure controllers are recorded at 1 Hz during an experiment.

Once the confining stresses have been applied, the fracturing fluid is injected into the central wellbore by a syringe pump at a constant flow rate (in the range 0.001–107 mL/min). The injection system uses an interface vessel to avoid filling the pump with the fracturing fluid as shown in Figure 1. Prior to the initiation of the fracture, the fracturing fluid is compressed as the pressure rises. Upon fracture initiation, for low viscosity fluids, the volume compressed during the pressurization phase can be suddenly released. Such a fast fluid release can lead to a fast transient growth, and even an unstable episode when the fluid is inviscous (Lecampion et al., 2017; Lhomme, 2005). For example, using water, such a compressibility effect can result in a growth of the fracture over 10 cm in a few seconds. In order to properly image fracture growth, such an early time effect associated with compressibility must be reduced at maximum. To do so, we use glycerol with a viscosity of $\mu = 0.6$ Pa s as the fracturing fluid. More importantly, a needle valve is placed in the injection line close to the well-head to damp any sudden fluid release associated with compressibility upon fracture initiation (as described in Bunger and Detournay (2008) among others). We record the fluid pressure (via HYDAC HDA 4846-B-600-000 pressure gauges) upstream and downstream of the valve located near the well-head at a sampling rate of 1 Hz.

An active acoustic imaging system is integrated into the loading platens to monitor the spatiotemporal evolution of the fracture (Figure 1). The acoustic array consists of 64 piezoelectric transducers with 32 acting as sources and 32 as receivers, of which 10 are shear wave transducers and 54 are longitudinal wave ones. Aluminum platens with holes act as placeholders for the acoustic transducers (note that we place the shear wave transducers in a way that the facing transducer pair shares the same polarization direction). A spring is placed at the back of the transducers to ensure that they do not carry the confinement applied to the aluminum platens. A couplant is put between the transducers and the rock sample for good acoustic contact. The transducers are custom-made units

Table 2
Sample Dimensions and Acoustic Wave Velocities

	v_p (m/s)	v_s (m/s)	Block size (mm)	Notch height (mm)
GABB-001	6679.0 ± 113.2	3668.5 ± 41.3	250 × 250 × 251	128.5
GABB-003	6791.3 ± 14.2	3722.7 ± 43.2	250 × 249 × 250	125
GABB-005	6743.8 ± 149.5	3678.0 ± 122.8	250 × 250 × 251	126
GABB-006	6734.5 ± 168.4	3668.9 ± 196.5	250 × 250 × 249	124

Note. v_p and v_s are measured on the block during the pressurization phase prior to fracture initiation. The mean and standard deviation are calculated based on vertical and horizontal ray paths measured during the first 10 acoustic scans (16 vertical ray paths for the calculation of v_p and five horizontal ray paths (in the North-South and East-West directions) for v_s). The block dimensions are reported in the three directions: North-South (N-S) × East-West (E-W) × Top-Bottom (T-B). The notch height is the vertical position of the notch taken from the bottom of the central wellbore.

from Olympus NDT, with disk-shaped active elements, 9.5 mm in diameter, and with a frequency response centered on 1 MHz. In practice, we generate a Ricker excitation signal (Ricker, 1951) at a central frequency of 750 kHz with a single-channel function generator board included in a National Instruments control system. This low-voltage signal is then amplified by a 55 dB high-voltage amplifier, in order to get a final amplitude of $\sim 350 V_{pp}$. The high-voltage signal is then routed through the multiplexer in order to excite sequentially the source transducers. The function generator sends excitation signals at 2 kHz repetition rate, and simultaneously generates a trigger pulse that starts the recording of all 32 receiver transducers at 50 MHz sampling rate via a 32-channel acquisition board. For each channel, 8,000 points are recorded, resulting in 160 μs of recording time. The time to switch between sources is limited by the internal electronic of the multiplexer, we thus repeat each shot 50 times for each source and stack the data to improve the signal-to-noise ratio. In fine, spanning of the 32 sources defines an acoustic scan which takes about 2.5 s. We typically repeat an acoustic scan every 4 s during the fracture growth. Repeating scans are also performed during the pressurization phase prior to fracture initiation. These early scans performed before any fracture(s) has initiated, allow to measure the acoustic wave velocity of the specimen along all the possible ray paths thus providing an estimate of sample heterogeneity in an acoustic sense at 750 kHz. The mean and variance of the measured acoustic velocities for the different specimens are reported in Table 2, which corresponds to a wavelength of around 9 mm for compressional waves. More details of the experimental setup and an example of the excitation signal waveform is reported in Supporting Information S1.

2.1. Methods

The acoustic monitoring methods used in this paper are described in details in Liu et al. (2020) (where one of the experiments (GABB-001) presented was used to document the reconstruction methods). We briefly recall below the main features of the monitoring methods for clarity.

2.1.1. Reconstruction of the Fracture Front Geometry From Scattered Waves

From the record of acoustic scans at repeated times during the experiment, subtracting from a scan at a given time a reference scan allows to eliminate the direct wave arrival and clearly visualize the arrivals of different scattered waves (see Liu et al. (2020) and Supporting Information S1). Using the manually picked arrivals of the scattered waves of different combinations of source-receiver pairs then allows for the reconstruction of the fracture front geometry. We reconstruct the fracture geometry using different geometrical models (ellipse, circle with or without any inclination). We rank these different geometrical models via their Bayes factor (assuming equiprobable models) in the context of a Bayesian inversion (Tarantola, 2005). This inversion is repeated for every acoustic scan independently. This ultimately provides an estimate of the time evolution of the fracture geometry, in particular the scattered fracture radius R_s over the entire experiment duration.

2.1.2. Fracture Opening Estimation

We estimate the fracture width w from compressional waves transmitted across the fracture plane between two facing transducers. For a plane wave having a perpendicular incidence with a fluid-filled slot (of constant aperture which is fully open), the transmission coefficient is known analytically and depends on the acoustic properties of the rock, fluid, and the unknown thickness of the fluid film. The inversion is performed in the Fourier domain by minimizing the difference between the FFT of the signal at the time of interest with the reference signal (prior to fracture initiation) convoluted with the transmission coefficient as a function of the unknown fluid thickness layer (see more details in Supporting Information S1). This method first pioneered in Groenenboom and Fokkema (1998) allows measuring fluid film thickness much smaller than the acoustic wavelength. This technique has been shown to compare well with optical measurements for hydraulic fractures propagating in transparent materials (Kovalyshen et al., 2014). We assume that the fracture is fully open and full of fluid, and refer to this fluid film thickness as the fracture width thereafter. We only use facing transducers satisfying the

Table 3
Experimental Parameters for Hydraulic Fracture Test Using Glycerol as Fracturing Fluid in Zimbabwe Gabbro

	μ (Pa · s)	σ_3 (MPa)	$\sigma_1 = \sigma_2$ (MPa)	Injection rate Q_o (mL/min)	System compressibility U (mL/GPa)
GABB-001	0.6	0.5	10.5	0.2	217.3
GABB-003	0.6	10	20	0.08	301.0
GABB-005	0.6	5	15	0.04	222.2
GABB-006	0.6	10	20	0.04	225.9

Note. The system compliance U is estimated from the pressurization phase of each experiment (prior to initiation).

normally incident plane-wave assumption to invert for fluid film thickness/fracture width. Of course, this estimate stems on the assumption of a locally planar fluid-filled fracture.

The accuracy of the width measurement with such a method can be partly estimated for a given experiment by inverting transmitted waves for several acoustic scans at the beginning of the test, prior to any fracture initiation. Such an estimate relates solely to the acquisition noises. We obtain 1–3 μm for most facing transducer pairs in the gabbro hydraulic fracture experiments reported here (see Figure 8).

This fracture width estimation using transmitted waves is restricted to longitudinal waves. We also monitor the changes of the acoustic amplitude for facing shear waves transducers comparing the waveform at a given scan with that of an initial acoustic scan at the beginning of the test (see more details in Liu et al. (2020) and Supporting Information S1). This provides additional qualitative estimate of fracture growth.

2.1.3. Post-test Imaging

We cut the specimen after the test. Two types of measurements are then performed: (a) micro-CT scans of subsample of the specimen containing part of the fracture, (b) a part of the fractured area (typically a quarter) is pulled apart, the roughness of the corresponding two surfaces is then measured. The microtomograph images were acquired at the PIXE Ultratom micro-CT platform at EPFL, resulting in a 15 μm voxel size resolution. The fractured surfaces topography was mapped using an optical profilometer (VR-3200, Keyence Corporation, Japan). For each surface, we measure two areas at two different resolutions: an area around 90 × 90 mm^2 is mapped at a spatial resolution of 47.006 μm/pixel (referred to as coarse), and a wide area of a 25 × 25 mm^2 is mapped at a resolution of 14.777 μm/pixel (referred to as fine). The surface roughness profiles are then analyzed by first removing the linear tilt of the whole surface. We then compute different statistics such as the root-mean-square (RMS) roughness, and the ratio between the "real" rough surface area and the nominal surface area in the assumption of a flat smooth fracture $A_{\text{rough}}/A_{\text{nominal}}$. The rough fractured area is obtained based on a linear interpolation of the measured roughness profiles, and is of course strongly influenced by the spatial resolution of the roughness measurement.

2.2. Experimental Design

Following LHFM (Detournay, 2016; Savitski & Detournay, 2002), the fluid pressure distribution inside a hydraulic fracture is spatially uniform (but varies in time) only in the so-called toughness dominated regime. Focusing on that particular growth regime will allow us to estimate the apparent fracture energy from the measurements of the evolution of the fluid pressure, reconstructed fracture front, and width measurements at the location of some source-receivers transducers pairs. We thus designed the experiments targeting the toughness propagation regime, using scaling relations for a single planar radial hydraulic fracture growth accounting for the system compressibility (Lecampion et al., 2017). These scaling relations are functions of rock, fluid properties, and test condition parameters, namely $\mu' = 12\mu$ where μ is the fluid viscosity, $E' = E/(1-\nu^2)$ the plane-strain Young's modulus, K_{Ic} the rock fracture toughness, Q_o the injection pump rate, and U the volumetric injection system compressibility and σ_3 the minimum confining stress. We refer to Lecampion et al. (2017) for details of the evolution of a radial hydraulic fracture and the different scaling laws (see also Detournay (2016) and Bunger et al. (2005) for laboratory hydraulic fracturing tests design).

In order to achieve toughness dominated growth while allowing for a sufficiently long duration of fracture growth over the specimen size to properly monitor its spatiotemporal changes, we use glycerol as a fracturing fluid with submilliliters per minute injection rate. In addition, we have put a needle valve in the injection line to control the flux entering the fracture after fracture initiation. In our study, we keep a biaxial state stress ($\sigma_1 = \sigma_2$) and the same magnitude of deviatoric stress $\sigma_1 - \sigma_3 = 10$ MPa for all tests. The configuration of the different experiments is summarized in Table 3. We further quantify in Section 4.1, the actual ratio of fracture energy over fluid viscous energy directly from our experimental results and verify that the fracture growth achieves the targeted toughness regime.

Due to the rather large average grain size of Zimbabwe gabbro (3 mm) compared to sample dimensions, it is likely that a large fracture process zone exists during these tests. Approximating such a process zone via a cohesive zone model (Anderson, 2017), we obtain a cohesive zone length scale L_{coh} and a time scale t_{cm} associated with the nucleation of the completely separated fracture (Garagash, 2019; Liu & Lecampion, 2021):

$$L_{coh} = \frac{K_{Ic}^2}{\sigma_c^2}, t_{cm} = \frac{E'^2 \mu'}{\sigma_c^3} \tag{1}$$

where σ_c is the material peak cohesive strength. Approximating $\sigma_c = 16$ MPa (Lama & Vutukuri, 1978) by the tensile strength of gabbro, and taking properties from Table 2, we obtain $t_{cm} = 21.1$ s and $L_{coh} \approx 0.03$ m. The small value of t_{cm} does not ensure a negligible influence of nonelastic processes, since plane-strain numerical simulations have notably shown that—especially for toughness dominated growth—the effect of the cohesive zone remains important even at ~100 times t_{cm} (Liu & Lecampion, 2021), which covers the fracture propagation time observed in our study (Table 3). Moreover, this value of the cohesive zone length scale is nonnegligible compared to the fracture extent, and implies a possibly significant effect on the fracture growth. Theoretical studies point out that the fracture growth under the influence of a process zone strongly depends on the confining stress ratio σ_3/σ_c (Liu & Lecampion, 2021). However, the correlation with the confining stress might not be observable in our experiments due to a relatively smaller range of σ_3/σ_c applied.

3. Results

The flow rate entering into the fracture is different from the pump injection rate Q_o during an initial transient phase after fracture initiation (Lecampion et al., 2017), resulting from the instant release of the fluid volume compressed in the injection line prior to fracture initiation. The presence of a needle valve in the injection line helps prevent any instability and regulate the entering fluid flux. Using volume conservation in the injection system, one can estimate the flow rate $Q_{in}(t)$ entering the fracture (and the accumulated injection volume V_{in}) as follows:

$$Q_{in} \approx Q_o - U\frac{\mathrm{d}p_{\text{upstream}}}{\mathrm{d}t}, V_{in}(t) = \int_0^t Q_{in}(\tau)\mathrm{d}\tau \tag{2}$$

where p_{upstream} is the fluid pressure measured upstream the needle valve and U is the overall volumetric compressibility [V/Pressure] of the injection system. Such an estimate neglects the effect of the volume of fluid downstream of the valve which is orders of magnitude smaller than the fluid volume in the upstream part of the injection line. Prior to fracture initiation, $Q_{in} = 0$, such that the pressurization of the system allows to directly measure the system volumetric compressibility U knowing the injection rate Q_o. This value can slightly change from experiment to experiment due to the length of the injection tube used (see Table 3). After the determination of U, the exact injection volume entering the fracture $V_{in}(t)$ can be readily estimated at any time from the measurement of the upstream pressure using Equation 2.

We report the time evolution of the fluid pressure, the accumulated injection volume as well as the fracture radius inverted from scattered waves in Figure 2 for GABB-001 (see Supporting Information S1 for similar plots for GABB-003, GABB-005, and GABB-006). When the fracture growth initiates from the notch, we observe a decrease in the volume of the top-bottom flat jacks and a drop in the pressure gauge located downstream of the needle valve. This allows us to consistently detect fracture initiation. The upstream pressure may then either continue to increase for some time when the needle valve is over-constrained (this is the case for GABB-001 and GABB-005) or directly decreases with time when the needle valve is more opened (for GABB-003). The downstream pressure drops significantly upon fracture initiation. A kink is visible in the volume change of the flat jacks pressure-volume controller at a later stage in the experiment as shown in Figure 2. This corresponds to the time at which the fracture front reaches the end of the specimen, and is consistent with the inversion of the scattered front from acoustic waves. Different net pressures $p = p_f - \sigma_3$ at the fracture initiation (from 14 to 22 MPa) have been observed in these four experiments which all exhibit an average fracture front velocity in the range 0.1–0.8 mm/s (see Table 4).

Note that a single fracture front was observed in all these hydraulic fracture experiments from the acoustic scattered waves. In addition, the transmitted signal across the fracture plane did not drop and regain its strength

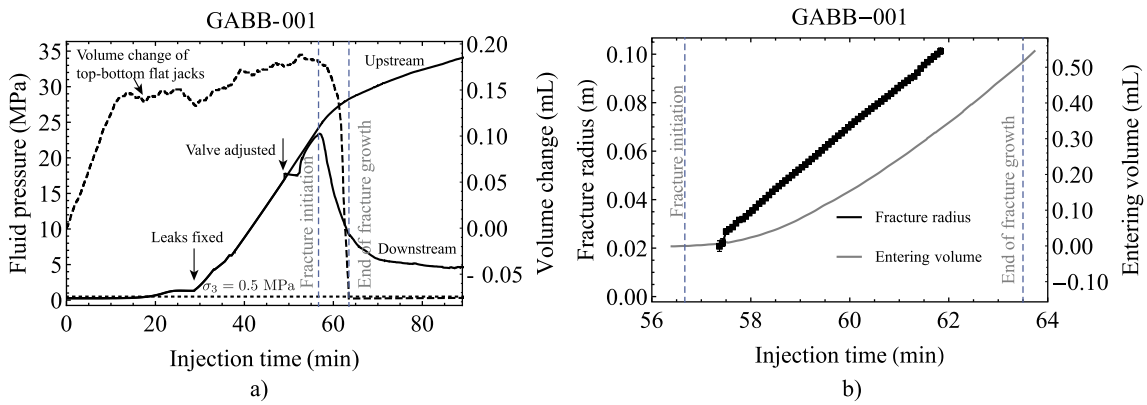

Figure 2. GABB-001: evolution of (a) injection pressure, (b) estimated fracture radius R_s (from scattered waves arrival) and flux entering into the fracture. The vertical lines indicate, respectively, the time of fracture initiation and the time at which the fracture reaches the block boundaries.

with time as typically observed when a fluid lag is present. This strongly points to the absence of a fluid lag in that toughness dominated experiments as expected from their design. We refer to Liu et al. (2020), Liu (2021), and Liu and Lecampion (n.d.) for clear examples of the effect of a fluid lag on acoustic measurements (both scattered and transmitted waves).

Bayesian analysis of the inversion favors a radial scattered fracture front rather than an elliptical one for all experiments except for GABB-006 (in particular the fracture front geometry at the later stage of the propagation). However, we assume in the following the scattered front is radial with a fracture radius of R_s to simplify the LEFM analysis. It is worthy to notice that GABB-005 presents a significant drift of the scattered fracture center away from the wellbore during the fracture growth. The fracture center offset increases from 2 to 5 cm as the fracture grows in GABB-005, this offset is at most 1 cm throughout the fracture propagation for the other three experiments. We illustrate in Figure 10 the scattered fracture fronts at different times.

After the end of the test, we cut a quarter of the samples and visualize the created fractures. This notably allows us to quantify the overall inclination and geometry of the fracture. These are in line with the evolving fracture front reconstructed from the scattered acoustic waves, as shown in Figure 3. Note that the darker zones correspond to fluid invasion which may have happened after the experiments. The samples have been cut (and the photo taken) several days after the injection (25 days in the case of GABB-001) such that the extent of invasion cannot be directly attributed to leak-off during the experiments. Visual observations indicate that the fractures have all initiated from the notch except in experiment GABB-006 in which the fracture initiated 9.5 mm below the notch (note that this is in agreement with the reconstructed fracture path from scattering waves (Figure 3)). In that experiment (GABB-006), two fractures are actually visible from this position: one results from the injection period we analyze in this paper, and the second one has initiated during a second injection stage performed at a much larger rate following the first injection stage discussed here.

Table 4
Minimum Confining Stress σ_3, Net Pressure at Fracture Initiation, Mean Velocity of the Scattered Fracture Front, and Total Propagation Duration for the Different Experiments

	σ_3 (MPa)	$p_f - \sigma_3$ (MPa)	v (mm/s)	t_{prop} (s)
GABB-001	0.5	22.8	0.29	≈410
GABB-003	10	16.1	0.86	≈158
GABB-005	5	14.6	0.11	≈780
GABB-006	10	21.5	0.77	≈136

4. Analysis Based on LHFM

We now analyze further these experimental results assuming a planar hydraulic fracture under the hypothesis of LHFM. Furthermore, we will assume that the experiments can be considered as being in the toughness dominated propagation regime. We recall that, in that regime, viscous fluid flow dissipation is negligible and the fluid pressure is uniform (but not constant) inside the fracture. This drastically simplifies any further analysis. However, these assumptions must be taken with caution and require proper evaluations.

4.1. Validity of Toughness Dominated Growth

We verify the validity of the toughness dominated growth through the evaluation of the dimensionless toughness $\mathcal{K}_m$ for a radial hydraulic fracture

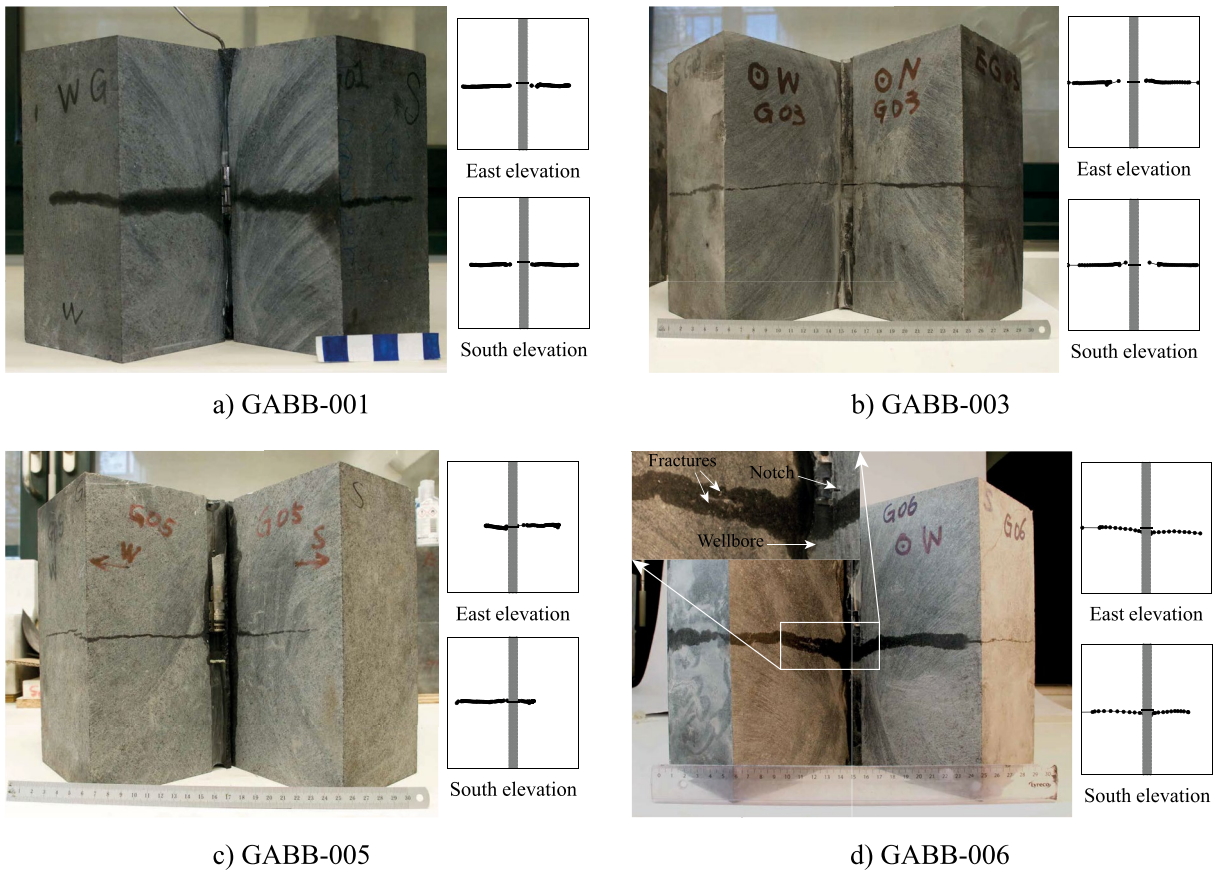

Figure 3. Comparison between the postmortem observation of gabbro samples after injections and the fracture paths reconstructed from scattering acoustic waves. The reconstructed fracture paths correspond, respectively, to the paths of the North-South and East-West cross sections passing through the center of the wellbore. They are obtained by joining the scattered fracture front reconstructed during the fracture growth.

(Savitski & Detournay, 2002). The dimensionless toughness $\mathcal{K}_m$ captures the ratio between the fracture energy and viscous flow dissipation. The expression of the dimensionless toughness for a constant rate (Savitski & Detournay, 2002) can be easily extended to a time-varying entering fluid volume $V(t)$

$$\mathcal{K}_m(t) = \frac{K_{Ic} t^{5/18}}{E'^{13/18} \mu'^{5/18} V(t)^{1/6}} \tag{3}$$

For a constant rate $V(t) = Q_o t$, the definition of $\mathcal{K}_m$ simplifies to the one first obtained in Savitski and Detournay (2002) pending a prefactor due to the removal of the coefficient $\sqrt{32/\pi}$ previously attached to the fracture toughness K_{Ic}. The definition used here ensures that the transition to the toughness dominated regime occurs when $\mathcal{K}_m \sim 1$.

Another estimate of dimensionless fracture toughness can be obtained from near-tip considerations. Garagash (2009) has shown that the dimensionless toughness for a finite fracture can be related to the near-tip behavior via its dependence on the current characteristic fracture length and velocity. Such a tip-based estimate does not depend on the knowledge of the injected volume and was shown to be equal to the dimensionless toughness obtained for finite fractures (radial and plane-strain) up to a prefactor associated with the relation between the characteristic length scale L and the actual fracture radius $R(t) = \gamma L(t)$. Taking here for γ the toughness dominated solution ($\gamma_k = 0.85/(\sqrt{32/\pi})^{2/5}$ in the toughness dominated scaling (Savitski & Detournay, 2002)), this near-tip estimate can be written as (Garagash, 2009)

$$\mathcal{K}_m^{tip}(t) = \frac{K_{Ic}}{E'^{2/3} \mu'^{1/3} (v_{tip}(t)/\gamma_k)^{1/3} (R(t)/\gamma_k)^{1/6}}, v_{tip} = \frac{\mathrm{d}R}{\mathrm{d}t} \tag{4}$$

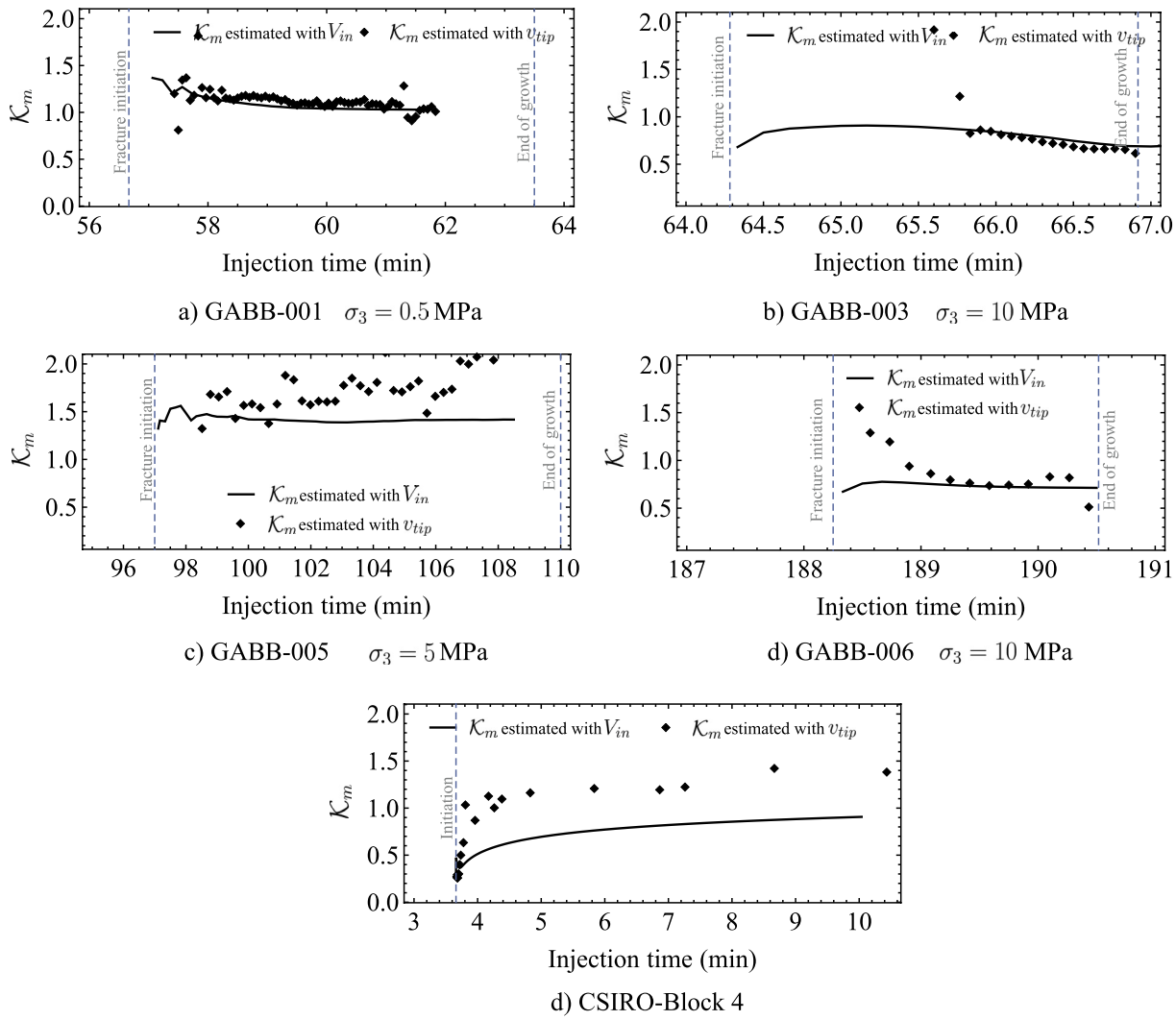

Figure 4. Time evolution of the dimensionless toughness $\mathcal{K}_m$. We take the toughness measured using the semicircular bending (SCB) method (Table 1) to evaluate $\mathcal{K}_m$: the black line indicates the results obtained using the estimated entering fluid volume V_{in} and the diamonds indicate those obtained from the scattered fracture tip velocity v_{tip}.

In Figure 4, we plot the evolution of the dimensionless toughness estimated by both Equations 3 and 4 using the material properties listed in Table 2. The estimation of $\mathcal{K}_m$ from Equation 3 is based on the estimated entering fluid volume, while when using Equation 4, we directly take the measured fracture radius from scattered waves $R = R_s$ and its time-derivative (we recall that the subscript s indicates that the fracture radius is estimated from scattered waves).

We observe from Figure 4 that these two estimates are of similar magnitude—especially at later times. The estimated $\mathcal{K}_m$ for these different experiments lies in a range [0.6, 2]. Theoretical predictions (Savitski & Detournay, 2002) using a first-order correction to obtain the hydraulic fracture growth solution for small dimensionless viscosity $\mathcal{M}_k = \mathcal{K}_m^{-18/5}$ have indicated that the solution is within 1% of the toughness dominated regime for $\mathcal{K}_m \geq 1.10$. Actually, the error evolves as $\pi^{9/5}/512\mathcal{K}_m^{-18/5}$ (the coefficient $\pi^{9/5}/512$ comes from the use of an adapted toughness parameter $K' = \sqrt{32/\pi}K_{Ic}$ in Savitski and Detournay (2002)), such that for the lowest value of dimensionless toughness observed here, $\mathcal{K}_m = 0.6$, the growth is only 9% off the toughness dominated regime. Moreover, the limit for toughness dominated growth ($\mathcal{K}_m \geq 1.10$) can actually be relaxed in the presence of a finite wellbore borehole which removes the viscous logarithmic pressure singularity at the inlet. For example, for a borehole of 4.2 mm in radius and a notch of 6 mm in radius, the actual minimum value of $\mathcal{K}_m$ for pure toughness

dominated growth has been found to relax to $\mathcal{K}_m \geq 0.92$ in experiments (Bunger, 2006). It is worth noting that in all experiments presented in this paper, the wellbore radius is around 8 mm and the outer notch radius is around 10.5 mm which would clearly remove the inlet logarithmic singularity. In Figure 4, we have also reported the dimensionless toughness estimates for another experimental data set performed in a brittle transparent PMMA specimen in the toughness dominated regime (CSIRO-Block 4 test). The estimate of toughness from the injected fluid volume is actually in the lower end of toughness dominated ($\mathcal{K}_m \sim 0.7$). Nevertheless, this test is properly reproduced by LHFM prediction in the toughness dominated regime (see Lecampion et al. (2017) for details). We can therefore conclude that all experiments reported here are in the toughness dominated regime and as such the fluid pressure can be approximately considered uniform inside the fracture with at worst 9% deviation (most likely less).

The fluid pressure is spatially uniform inside the fracture when the fracture growth is dominated by the fracture toughness. For such a loading, the fracture width $w(r, t)$ and the fracture volume $V(t)$ can be expressed in function of the fluid pressure and fracture radius from the well-known elastic solution of a radial crack in an infinite elastic medium (Sneddon, 1946)

$$w(r,t) = \frac{8}{\pi}\frac{(p_f(t)-\sigma_3)}{E'}\sqrt{R(t)^2 - r^2} \tag{5}$$

$$V(t) = \frac{16}{3}\frac{(p_f(t)-\sigma_3)\,R(t)^3}{E'} \tag{6}$$

Under the assumption of LEFM, the material fracture toughness K_{Ic} must equal the mode I stress intensity factor K_I during quasi-static growth. The stress intensity factor is known in closed form for a uniformly loaded radial fracture in an infinite medium (Tada et al., 1973), such that the propagation condition reduces to

$$K_{Ic} = K_I = \frac{2}{\sqrt{\pi}}(p_f(t)-\sigma_3)\sqrt{R(t)} \tag{7}$$

Replacing the net pressure by the expression of the stress intensity factor Equation 7 which equals the material toughness during propagation, we can express the width profile and the fracture volume as a function of the fracture toughness

$$w(r,t) = \frac{4}{\sqrt{\pi}}\frac{K_{Ic}}{E'}\frac{1}{\sqrt{R(t)}}\sqrt{R(t)^2 - r^2} \tag{8}$$

$$V(t) = \frac{8\sqrt{\pi}}{3}\frac{K_{Ic}}{E'}R(t)^{5/2} \tag{9}$$

These different expressions will allow us to evaluate the same quantities from independent measurements. In the following, we use a subscript s to represent estimates obtained from the scattered fracture extent, and a subscript w for estimates obtained from the acoustic width profile measurement.

Acknowledging that our specimens have limited dimensions, we perform a first-order correction for the apparent fracture toughness/stress intensity factor and the fracture volume using the known elastic solution for a centered radial fracture in a cylindrical specimen with the same radius as the block dimension $L_b = 0.125$ m (Tada et al., 1973). Such a correction pertains to a simple multiplication of the stress intensity factor and elastic volume by correcting factors Y_k and Y_v depending on the ratio of fracture radius to specimen dimension. We recall these correcting factors in the Appendix A. Although not exactly corresponding to the geometry of our cubic samples, this correction is a first-order approximation which likely becomes inaccurate when $R/L_b \to 0.8$ as the cubic geometry will start to have a significant influence.

4.2. Estimated Fracture Volume (From $p(t)$ and $R_s(t)$) Versus Entering Fluid Volume

During propagation, from the estimated fracture radius from scattered waves $R = R_s$ and the downstream pressure measurement (at the same time), we can compare the elastic estimate of the fracture volume $V_s(t)$ with the

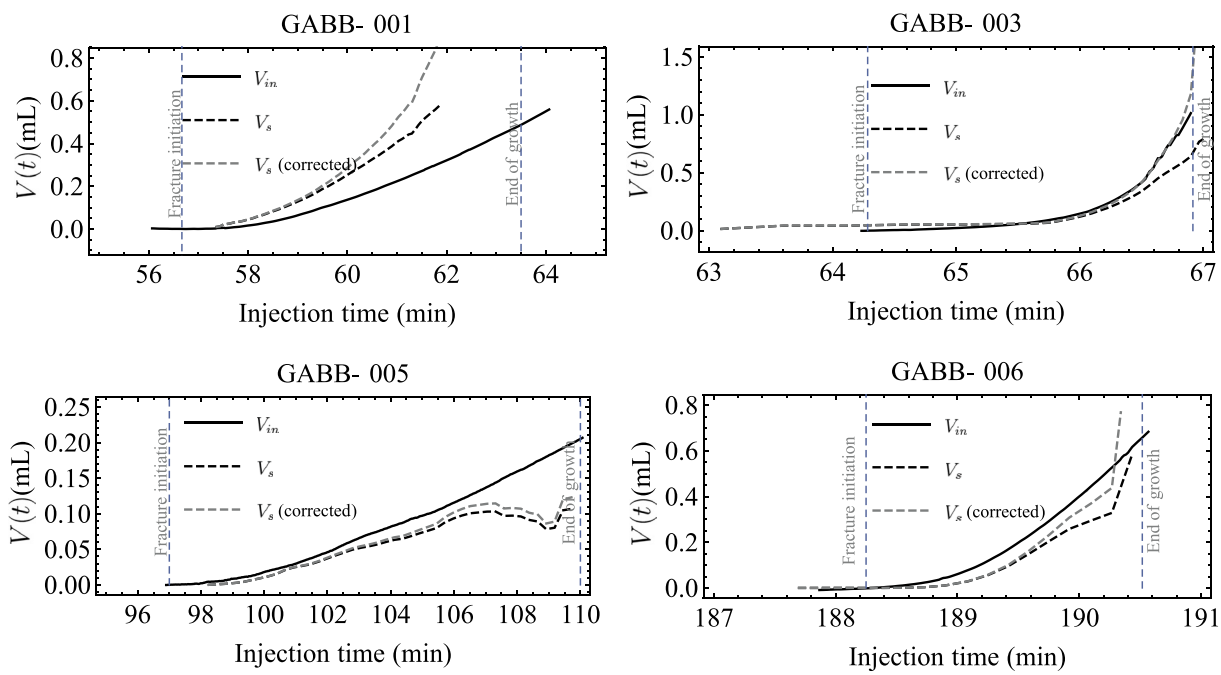

Figure 5. Comparison of the entering fluid volume V_{in} (estimated from the pressure record and injection compliance) and the estimated fracture volume from elasticity and recorded downstream pressure $V_s(p, R_s)$ (assuming a toughness dominated radial hydraulic fracture). V_s(corrected) is the corrected V_s on the account of the boundary effect of sample dimensions by approximating the growing hydraulic fracture as a centered radial fracture propagating in a cylindrical sample with the same radius as the block dimension $L_b = 0.125$ m.

injected fluid volume $V_{in}(t)$ estimated from the measured pressure and injection rate from Equation 2. The results are reported in Figure 5.

In GABB-003, the entering fluid volume V_{in} matches very well with the estimated fracture volume V_s at all times. Although, the fracture volume is slightly lower than the entering fluid volume, $V_{in} \sim V_s$ for most of the propagation in GABB-005 and GABB-006. In GABB-005, the fracture center drifts away from the wellbore as shown in Figure 10. The boundaries of the specimen likely have a stronger influence on the volume estimated via Equation A2 (and thus underestimate fracture volume in the presence of finite boundaries). In addition, the applied minimum stress σ_3 is also lower closer to the boundary due to the geometry of the loading system (Moukhtari, 2020). As a result, the estimated fracture volume when the fracture front comes close to the specimen boundary is likely severely underestimated for GABB-005 as shown in Figure 5.

In GABB-006, the fracture initiates at the bottom of the pressurized interval instead of the tip of the notch. The fracture path thus curves and reorients in the near wellbore as can be observed in Figure 3. Note that the propagating net pressure is larger which is consistent with a curved fracture. Assuming a planar radial fracture would underestimate the fracture area and thus volume, an effect that may be only partially compensated by a higher net pressure. It is possible that a small amount of fluid leaks off in some microcracks/pores around the fracture and thus lowers the estimated fracture volume. One should keep in mind that fluid leak-off has also the tendency to increase the fracture net pressure, and that poroelastic back-stress due to pore-pressure increase tends to lower fracture width. A larger net pressure may thus possibly artificially increase the fracture volume estimated from the elastic volume relation Equation 6 which does not account for any poroelastic back-stress (for the same fracture radius). The existence of leak-off cannot be ruled out but is difficult to quantify further.

Clearly different from other experiments, in GABB-001, the estimated fracture volume V_s is larger than the injected fluid V_{in} volume by around 80% and even more for volume corrected with the boundary effects (see Figure 5). Any significant difference in elastic properties is highly unlikely as the acoustic velocities recorded under confinement are similar between these four samples (see Table 2). No leaks are observed during the injections. Moreover, the leak-off conditions should not vary significantly from the other three experiments. This experiment (like GABB-006) also exhibits a larger net pressure than that of GABB-003 and GABB-005. Two

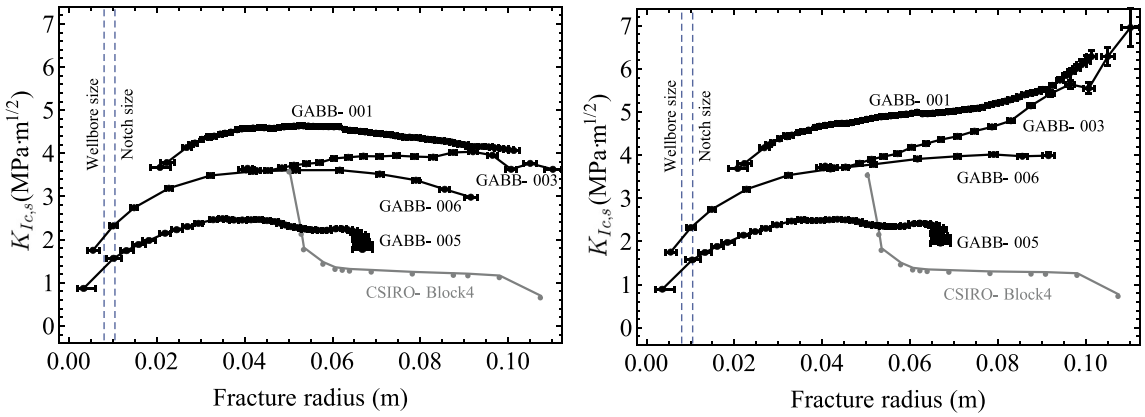

a) Without correction for boundary effects

b) With correction for boundary effects

Figure 6. Evolution of the estimated apparent toughness $K_{Ic,s}$ with fracture radius R_s (a) without and (b) with an approximate correction of the boundary effect. The experiment performed in brittle PMMA (CSIRO-Block 4) is displayed for comparison (the drop of $K_{Ic,s}$ is associated with the end of the viscous/compressibility effects in that experiment for which we plot data only for $\mathcal{K}_m > 0.5$—see Figure 4).

explanations are possible: (a) the existence of an entry-pressure loss due to some restrictions between the pressure gauge and the fracture inlet, (b) partly segmented fracture areas which are not completely connected inside the fracture leading to the requirement of a larger fluid pressure to propagate the fracture.

4.3. Apparent Fracture Toughness From $p(t)$ and $R_s(t)$

We can directly use the recorded downstream pressure and fracture radius R_s to estimate an apparent mode I fracture toughness $K_{Ic,s}$ using Equation 7 under the assumption of toughness dominated growth.

We plot these estimates of the apparent toughness as a function of the estimated fracture radius in Figure 6a without boundary correction (Equation 7), and in Figure 6b with boundary correction (Equation A1). The apparent toughness varies significantly between experiments, but also during an experiment. Except for GABB-005 (which we discuss separately later), the estimated apparent fracture toughnesses are much larger than measured on semicircular bending tests ($K_{Ic} \approx 2.8$ MPa · m$^{1/2}$). For comparison, we have also displayed the apparent toughness estimated in the same way (from the measurement of pressure and radius) for the CSIRO-Block 4 experiment performed in a brittle PMMA in the toughness dominated regime (see Lecampion et al. (2017) for details). It is striking to see that for that experiment, after an initial decrease of $K_{Ic,s}$ associated with a strong compressibility effect at fracture initiation (which triggers a viscous pressure drop in the fracture), the value of estimated toughness tends to a constant very close to the material fracture toughness reported: $K_{Ic,s} \approx 1.3$ MPa · m$^{1/2}$ (Lecampion et al., 2017).

The evolution of the apparent toughness is similar for all the experiments performed in gabbro and significantly different than for the experiment in brittle PMMA. The apparent toughness first increases with fracture radius. Without accounting for the boundary correction (Equation A1), the apparent fracture toughness then decreases when the fracture reaches about half the specimen size. Such a decrease does not necessarily reflect the real evolution of $K_{Ic,s}$ as Equation 7 is only valid for an infinite elastic medium. Accounting for the boundary correction (Equation A1), the apparent fracture toughness is now always increasing (Figure 6b). Such a continuous increase of $K_{Ic,s}$ with the fracture extent possibly implies a continuous growth of the nonlinear effect and its associated energy dissipation in the solid.

Similar to the estimation of the fracture volume, the chosen boundary correction (which assumes a cylindrical shape for the specimen which is in fact rectangular) likely becomes inaccurate when the fracture radius reaches 9 cm and the shape of the external boundaries starts to matter. The correction applied also assumes that the fracture remains exactly centered during the whole experiment.

It is also worth noting that the reported estimation of $K_{Ic,s}$ assumes that the minimum confining stress σ_3 is uniformly applied on the fracture plane and equal to the flat jack pressure—which is not truly correct. There is a partial

loss of transmitted pressure due to the contact conditions between the flat jacks, spacers, and specimen surfaces (due to friction). Finite element simulations of the overall geometry (accounting for the platens transmitting the pressure and the finite specimen) have shown that for a hydrostatic loading condition $\sigma_1 = \sigma_2 = \sigma_3 = 20$ MPa, a stress attenuation of around 15% ($\sigma_3 \approx 17$ MPa) in an area around 60 mm is reported in the center plane of the sample (Moukhtari, 2020). Taking directly the flat jack pressures, we thus use an upper bound for σ_3 here, such that the reported apparent toughness is probably underestimated. This lower confinement may be on the other hand partly offset by a possible entry-pressure loss which would result in lower fluid pressure inside the fracture.

The apparent toughness estimated for GABB-005 is lower compared to other experiments. This can be explained by the fact that the fracture center in GABB-005 significantly drifts away from the central injection wellbore, and grows in an area where the applied confinement is lower. This experiment is affected very early on by the boundaries of the sample (see snapshots of the reconstructed fracture front in Figure 10), and the axisymmetric correction (Equation A1) is not sufficient to correct it. The reported values of $K_{Ic,s}$ for that experiment in Figure 6 are clearly underestimated as a result of this drift and the resulting lower confinement encountered by that fracture.

4.4. Apparent Toughness and Radius From $w(r, t)$

We can obtain another estimate of the fracture radius and apparent toughness using the fracture width measured from the acoustic transmission as described in Section 2.1.

Upon knowledge of the width measured from acoustic transmission at 16 top-bottom platens transducer pairs (compressional transducers only) forming a cross-like array (Figure 8), we invert Equation 8 for the fracture radius, fracture center, and the apparent toughness K_{Ic} using the elastic solutions (5). To do so, we perform a Markov-Chain Monte-Carlo sampling and estimate their associated uncertainties. Since the effect of the specimen boundary becomes significant when the fracture radius becomes large, we restrict this analysis to a time where the scattered fracture radius is about half of the sample dimension. This choice corresponds to a boundary correction factor for fracture toughness $Y_k < 1.1$ (see Appendix A) which indicates that the use of the infinite medium approximation is warranted. In addition, such an acoustic scan half-way through the propagation provides the maximum amount of available width measurements from transmitted waves—which would be too little for a robust inversion for smaller fracture radius.

We illustrate the width profiles and their associated fits in Figure 7 along the North-South, East-West axis for experiments GABB-001 and GABB-003 (see the corresponding results of GABB-005 and GABB-006 in Supporting Information S1). In addition to the measured and best-fit width obtained (black and gray continuous lines), we also report in dashed blue the width profiles predicted from the measurement of the fracture radius from scattered waves and the fluid pressure (as done in Section 4.2 for the estimation of fracture volume) as well as the width predicted using the fracture radius estimated from width and the fluid pressure measurement (dashed-black lines).

It is interesting to note that the measured width profile is not always completely concave: the width seems to be constrained at some transducer locations. The elastic prediction of the fracture width taking the recorded net pressure $w(p, R_w)$ is equivalent to the width obtained from the acoustic transmission only for GABB-003, while in the other experiments, $w(p, R_w)$ is always larger than the width measured via acoustics. Similarly, only for GABB-003, the width estimated from the scattered radius and the recorded net pressure is consistent—although lower—than the measured width.

We list the estimated values of the apparent toughness, fracture radius, and fracture center offsets in Table 5, and compare them with those obtained in Section. 4.3 for the same time. The fracture extent is larger than that measured from the scattering waves $R_w > R_s$ by a centimeter or more. The apparent fracture toughness is in the same order of magnitude as those obtained from Equation 7 albeit slightly smaller.

We also report in Table 5 the corresponding fracture volume from the fitted fracture width measurement V_w. It is always larger than the entering fluid volume V_{in} but also larger than the elastic estimate V_s from the radius reconstructed from scattered wave and the fluid pressure. This is likely associated with the nontotally smooth width profiles measured, and the fact that the width at locations apart from the 16 compressional facing transducer pairs array is likely smaller.

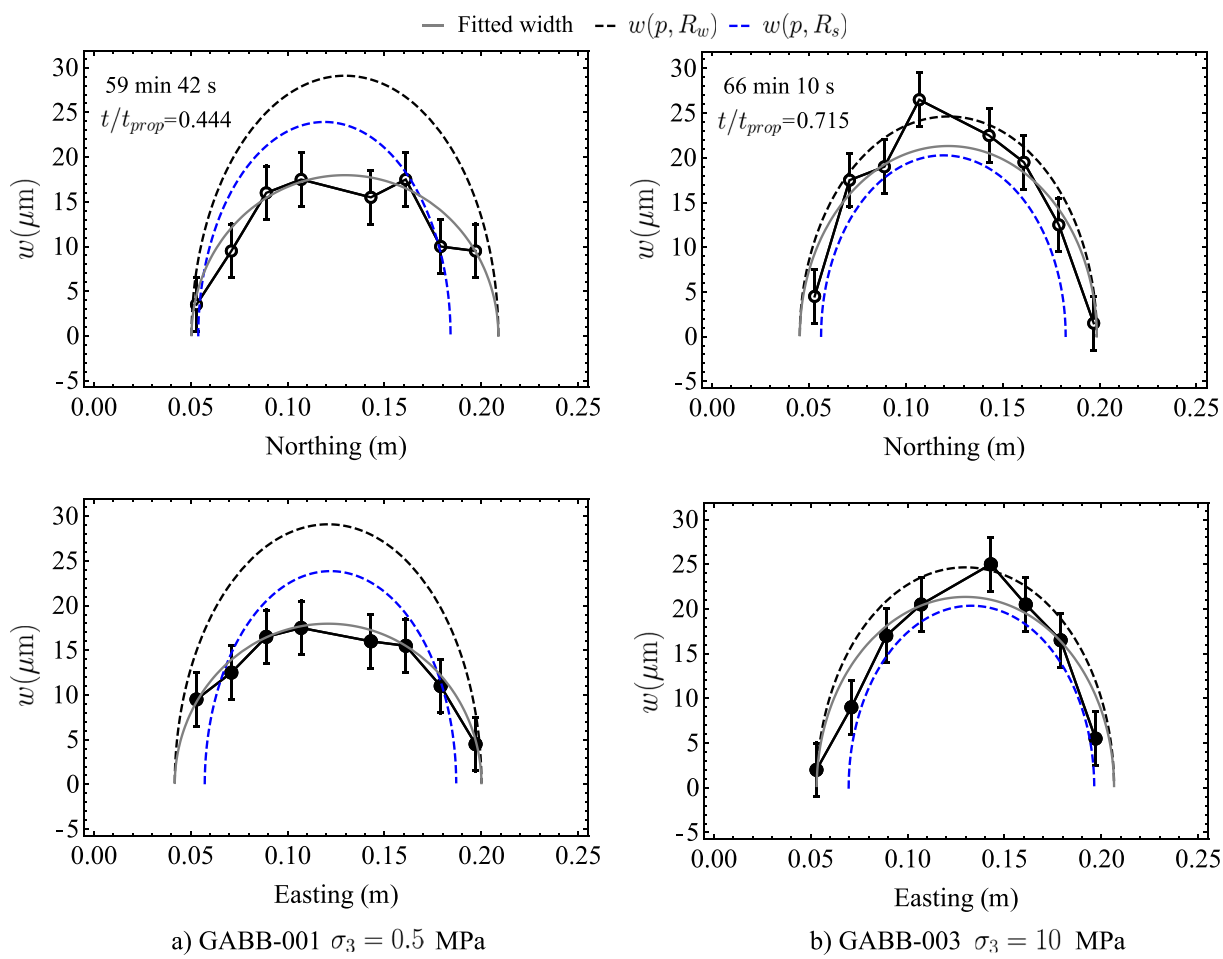

Figure 7. Measured fracture width for different source-transducers pairs. The filled and empty disks indicate, respectively, the width obtained from the *P* wave transducers in the East-West direction and the North-South direction (These directions are illustrated in Figure 1 in 3D and in Figure 10 in the top view of the rock sample). The dashed-black curve and blue curve correspond, respectively, to the elastic prediction using the recorded downstream pressure and the fracture radius fitted from the width profile R_w, and that using the recorded downstream pressure and the fracture radius obtained from scattering waves R_s. The gray curve corresponds to the best-fit linear elastic fracture mechanics (LEFM) profiles using Equation 8.

5. Discussions

Two observations in these experiments cannot be explained by the model of a smooth planar hydraulic fracture under the LHFM assumptions:

1. The apparent fracture toughness estimated (by different methods) from these hydraulic fracturing tests is significantly larger than the one measured from the semicircular bending test, and varies significantly between experiments.
2. Elasticity overestimates the fracture volume and width profiles (Figures 5 and 7, and Table 5), in particular for GABB-001 when assuming similar rock properties and leak-off conditions between experiments.

In the following, we discuss in more details the possible causes of such discrepancies.

5.1. Attenuation of Transmitted Waves Ahead of the Scattered Front

As already visible in Figure 7, the fracture radius reconstructed from scattering always appears smaller than the radius defined by the measurement of fracture width via transmitted waves. Indeed, we consistently observe amplitude attenuation in both shear and compressional transmitted waves, when the scattered fracture front has not yet reached the sight of the corresponding facing source-receiver pairs (see more details in Supporting Information S1). Fracture width is also detected prior to the arrival of the scattered front (see Figures 7 and 8, and other

Table 5
Estimates Obtained From the Fracture Width Measured via Acoustics (the Fracture Radius R_w, the Offset Distance of the Fracture Center Away From the Block Center Δx_w, the Apparent Fracture Toughness $K_{Ic,w}$, and the Fracture Volume V_w) and Those Obtained From the Scattered Fracture Radius and Fluid Pressure (R_s, Δx_s, $K_{Ic,s}(R_s, p_f)$, and the Fracture Volume V_s Without Boundary Correction)

Experiment	GABB-001	GABB-003	GABB-005	GABB-006
σ_3 (MPa)	0.5	10	5	10
Injection time	59 min 42 s	66 min 10 s	102 min 31 s	189 min 35 s
R_w (m)	0.079 ± 0.003	0.077 ± 0.004	0.084 ± 0.007	0.088 ± 0.009
R_s (m)	0.065 ± 0.0003	0.064 ± 0.0007	0.045 ± 0.0008	0.062 ± 0.0007
Center offset Δx_w (mm)	6.2 ± 0.6	5.7 ± 1.6	13.3 ± 0.4	24.9 ± 1.3
Center offset Δx_s (mm)	6.6 ± 0.6	9.7 ± 0.2	27.6 ± 0.7	11.4 ± 1.4
$K_{Ic,w}$ from Equation 8 (MPa · m$^{1/2}$)	3.08 ± 0.09	3.72 ± 0.16	1.88 ± 0.11	3.09 ± 0.20
$K_{Ic,s}$ from Equation 7 (MPa · m$^{1/2}$)	4.527 ± 0.0007	3.909 ± 0.001	2.434 ± 0.0009	3.611 ± 0.001
V_w from Equation 9 ($\times 10^{-7}$ m^3)	2.37 ± 0.30	2.64 ± 0.42	1.66 ± 0.42	3.07 ± 0.97
V_s from Equation 6 ($\times 10^{-7}$ m^3)	2.12 ± 0.03	1.73 ± 0.05	0.45 ± 0.02	1.48 ± 0.05
V_{in} ($\times 10^{-7}$ m^3)	≈1.19	≈2.37	≈0.58	≈2.53

examples in Supporting Information S1). It is therefore very likely that the scattering fracture front is somehow "lagging" behind the real physical fracture front. This mismatch possibly results from a systematic bias in the picking of the scattering wave arrivals associated with a low signal-to-noise ratio. Another possible explanation is that such attenuation is related to the presence of secondary fractures formed in a damage zone ahead of the fracture front. These secondary cracks may result from cleavage cracks formed ahead of the fracture front, which are then linked to the macrofracture by coalescence. Even though we do not observe any secondary cracks in microtomograph images (possibly due to the limited resolution), their presence cannot be completely ruled out.

To quantify this attenuation further, we postprocess our measurements of the width and scattered front in two ways. First, we pick the fracture opening w_a (a emphasizing its relation to acoustic attenuation) corresponding to the time at which the scattering front comes in the line of sight of the corresponding vertical transducer pairs. w_a thus characterizes the fracture width at which scattering appears. Second, we also estimate, the shortest (planar) distance ℓ_a between the scattering front and the location of a top-bottom transducer pair at the time where the fracture width starts to increase for that specific pair (Figure 8). This time is determined by the change of slope in the time history of measured fracture width for compressional wave transducer pairs (see Figure 8a), and by the start of amplitude attenuation for shear wave transducers (see Supporting Information S1 for more details). ℓ_a quantifies the mismatch between the fracture front reconstructed from scattering and either the real fracture front or at least the location where microdamage starts.

We summarize in Figure 9 the estimates of w_a and ℓ_a for all vertical acoustic transducer pairs in the four experiments. w_a vary from 0 to 20 μm for all four experiments, and is much smaller than the grain size and the fracture surface roughness. It remains of the same order of magnitude as the fracture extent grows away from the wellbore. The maximum ℓ_a varies from 2 to 7 cm between experiments. Although difficult to quantify, the error bar on these estimates is likely at least 5 mm. It is interesting to note that the difference ($R_w - R_s$) between the fracture radius estimates using, respectively, the scattering waves R_s and the width profile from acoustics R_w (estimated only at a single time) fall in the same range than ℓ_a. This tends to indicate that there is possibly a systematic bias in the picking of the scattered waves.

5.1.1. Implications

It is interesting to recall the order of magnitude of the expected fracture process zone in such gabbro using the classical cohesive zone model (see Section 2.2): $L_{coh} \sim 3$ cm for its size and $w_c \sim 10$ μm for the critical width. Although these orders of magnitude are in line with the measurement of ℓ_a and w_a, it is unclear if the attenuation of transmitted waves ahead of the reconstructed front clearly indicates a damage zone or if it is just related to the accuracy of the picking of the arrival of the scattered waves. Further investigations are thus required. Addition of passive acoustic monitoring would likely help to further decipher this point.

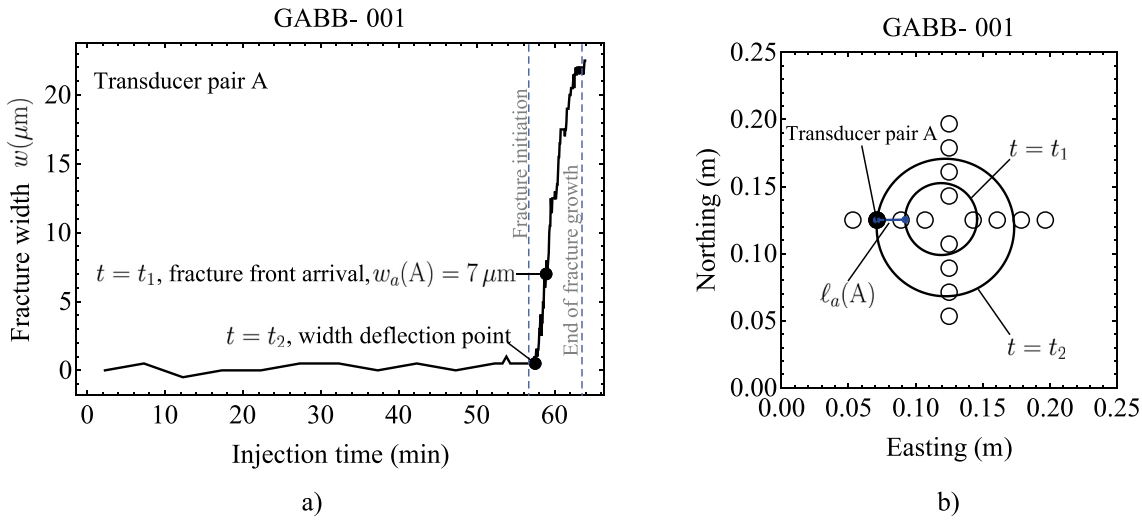

Figure 8. GABB-001: time evolution of the fracture width for one transducer pair, and illustration of ℓ_a and w_a for this transducer pair and its associated fracture front footprints. The inverted width in (a) prior to fracture initiation provides a measure of the expected accuracy.

Previous studies on fault activation experiments in granite (Aben et al., 2019) analyze the local change of elastic properties in the sample due to microcracking with acoustic wave velocities. They claim that the dissipation due to microcracking off the fracture plane takes a small portion (around 10%) of the fracture energy. Ritchie (2011) also points out that the toughening mechanism due to microcracking ahead of the fracture tip, is not dominant in rock materials, compared to fracture bridging. It is likely that the energy dissipation due to the presence of a damage zone around the hydraulic fractures is limited in gabbro as well—a point which we will further illustrate via postmortem micro-X-ray computer tomography images.

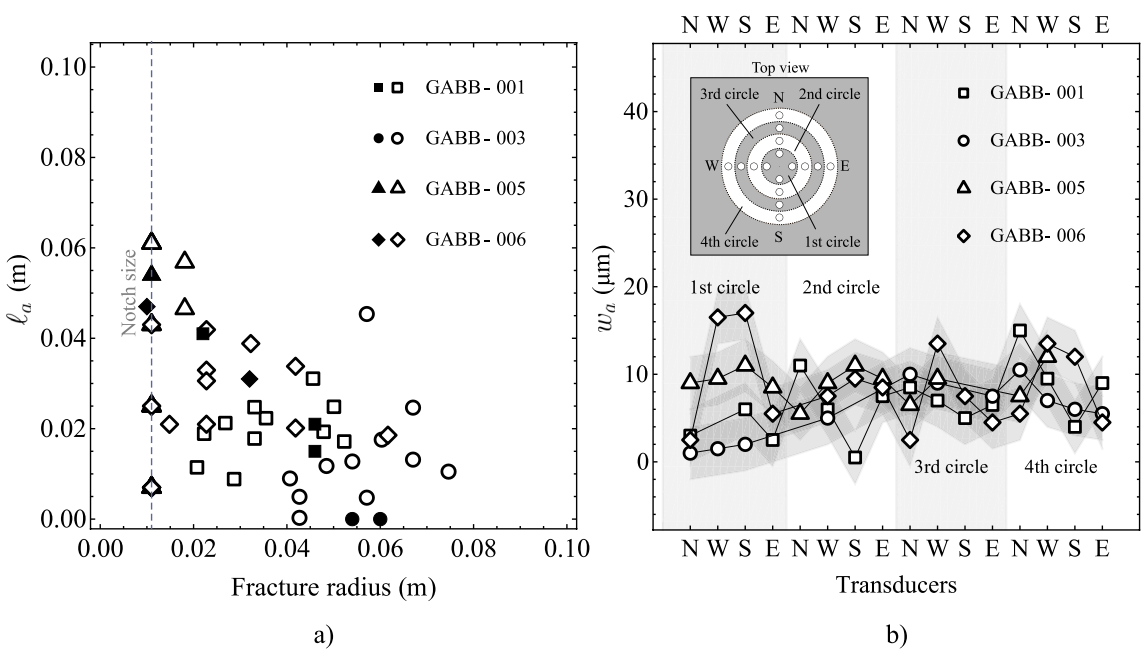

Figure 9. (a) Evolution of ℓ_a obtained from facing transducer pairs (empty markers indicate the *P* wave transducer pairs, and solid markers the *S* wave transducer pairs) as a function of fracture radius. ℓ_a quantifies the mismatch between the fracture front reconstructed from scattering and either the real fracture front or at least the location where microdamage starts. (b) Fracture width w_a of different transducers at the arrival of the scattered fracture front. The transducers are shown from the left to the right as the ones at the first circle of the transducers closest to the wellbore (in an anticlockwise direction) to the ones at the fourth circle farthest away from the wellbore (in an anticlockwise direction).

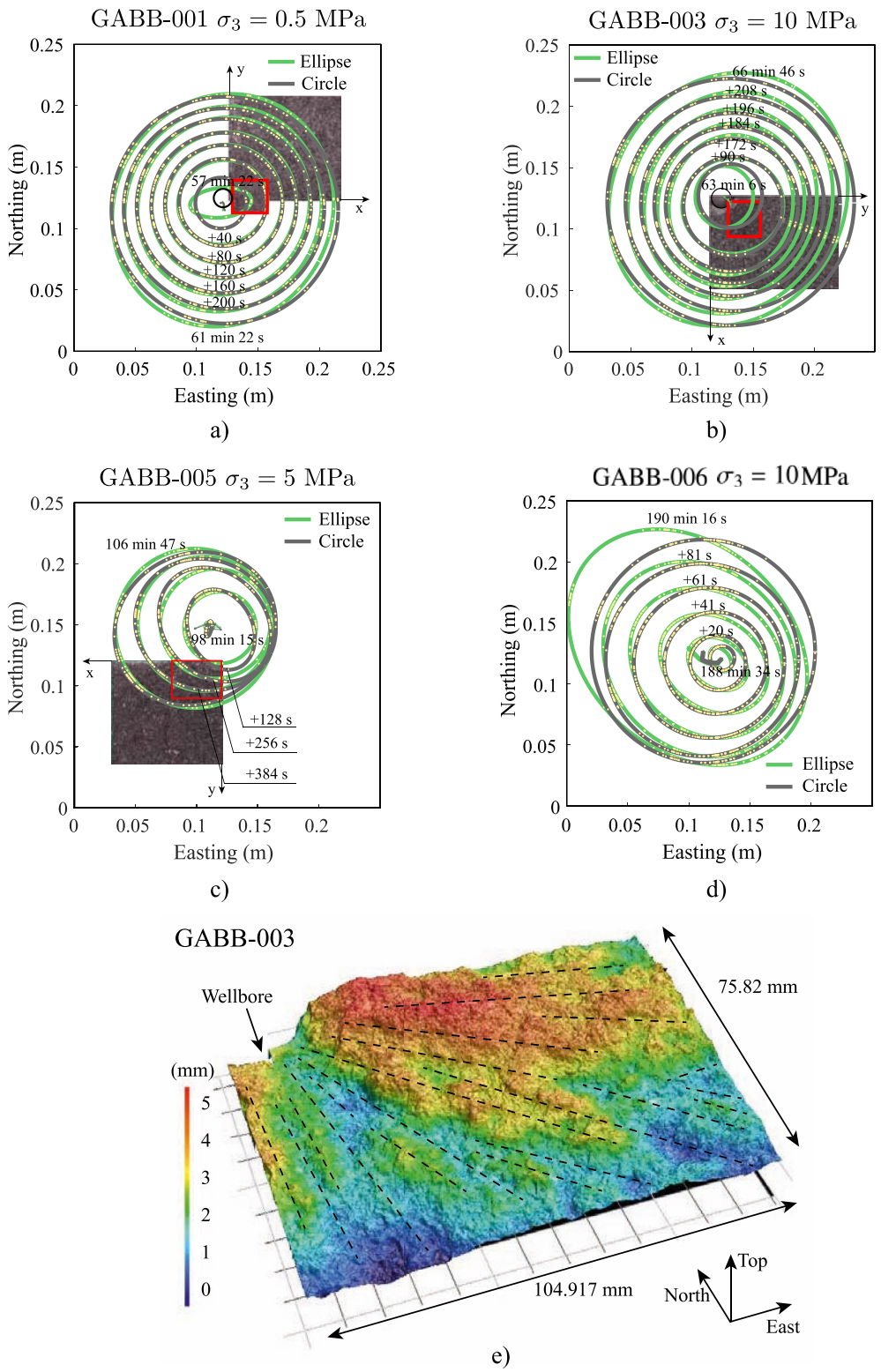

Figure 10. Top view of (a) GABB-001, (b) GABB-003, (c) GABB-005, and (d) GABB-006 with fracture footprints. We show the fracture footprints reconstructed from scattered waves assuming either an elliptical shape of the fracture or a circular shape. The yellow points on the reconstructed fracture front are the scattered points. The larger scanned area corresponds to the coarse mode measured with a resolution of 47.006 μm/pixel (indicated by the photo in the figure), and the smaller interest area indicated by a red rectangle corresponds to the fine mode measured with a resolution of 14.777 μm/pixel. (e) An illustration of the measured fracture roughness surface of GABB-003 after pulling out the two connected parts by force. The dashed lines indicate the rib markings which stem from the injection point and fan out (Bahat, 1991).

Table 6
Characterization of Subparts (See Figure 10 for Their Locations) of the Created Fracture Surfaces Roughness

Rock sample	σ_3 (MPa)	Spatial resolution	RMS (μm)	$A_{rough}/A_{nominal}$
GABB-001-NEB	0.5	Coarse	688.4	1.11
GABB-003-SEB	10	Coarse	773.7	1.12
GABB-005-SWB	5	Coarse	933.9	1.13
GABB-001-NEB	0.5	Fine	502.5	1.34
GABB-003-SEB	10	Fine	585.8	1.58
GABB-005-SWB	5	Fine	631.9	1.43

Note. RMS indicates the root-mean-square (RMS) roughness, $A_{rough}/A_{nominal}$ represents the ratio between the measured rough surface area and the nominal surface area in the assumption of a flat smooth fracture. "Coarse" corresponds to an area of around 90 × 90 mm^2 scanned with a resolution of 47.006 µm/pixel, while "Fine" corresponds an area of around 25 × 25 mm^2 with a resolution of 14.777 µm/pixel. NEB and SEB represent, respectively, the northeastern and the southeastern, part of the bottom fractured surface.

5.2. Fracture Overlapping and Bridging

All the samples remain connected after the test although a macroscopic fracture path is visible throughout the samples. Application of a load (with a hammer) was necessary in order to completely separate the fracture surfaces. This indicates the presence of a number of "unconnected" parts-bridges.

We first have a look at the separated fracture surfaces. They are all very rough. More interestingly, the surface roughness profiles for the GABB-003 exhibit rib markings from the injection origin and fanning outward (Figure 10d), while the other surfaces do not show any obvious rib markings.

These rough fracture surfaces may act as one of the toughening mechanisms for fracture growth: a rough fracture contains more fractured area than a smooth fracture, which leads to more energy dissipation in the fracturing process (Lawn, 1993). To be more specific, the fracture energy scales with the fractured area A when the energy dissipation solely comes from atomic debonding in the context of constant surface energy. As a result of Irwin's equation (Irwin, 1957), the apparent fracture toughness becomes proportional to the square root of the fractured area $K_{Ic} \sim \sqrt{A}$. We aim to quantify this toughening mechanism in parts of the specimens (Figure 10) by calculating the RMS of the roughness heights, and the ratio between the rough surface area and its nominal area in the assumption of a flat smooth fracture $A_{rough}/A_{nominal}$. As shown in Table 6, RMS is in the same order of magnitude as the grain size for all experiments and that no obvious correlation is found between roughness properties and the confining stress. A strong correlation, however, exists between the roughness properties and the size of the measurement region and its resolution: the roughness in a larger scan area tends to present a larger maximum variation from the average fracture surface, thus a larger RMS. The roughness measured with a high resolution tends to capture more local variations of the fracture path, thus a larger ratio between the rough surface area and its nominal area in the assumption of a flat smooth fracture $A_{rough}/A_{nominal}$. With the finest resolution, our measurement here suggests a maximum increase of the apparent fracture toughness of around 26% according to Irwin's relation. Accounting for this correction, the apparent fracture toughness is still far below the reported toughness in Section. 4.3. Moreover, this increase of the real fractured area is only partially responsible to the increase of the apparent toughness reported in these experiments since not all fracture surfaces are broken during fracture growth. Further investigation of these connected areas is essential.

We were able to core a few parts of some samples cut through by the fracture, and image them via X-ray computer tomography (micro-CT) without separating the fracture surfaces. These tomography observations indicate a complex fracture path located within a band of around 1–1.5 mm as can be seen from Figure 11. The thickness of this band is consistent with the average grain size and the RMS roughness reported in Table 6. Overlapping fracture segments exist widely as can be seen from the micro-CT images taken in two different directions. They are also accompanied by fracture bridging, where the fracture surfaces are not completely broken but bridged by some connected areas. Note that the rib markings of the fracture surface roughness profiles (Figure 10e) and the fracture overlapping are typical features of echelon cracks (Bahat, 1991).

It is well known in fracture mechanics that a small amount of mode mixity (II and/or III) can promote segmentation of the fracture front of an otherwise mostly mode I fracture in a number of adjacent segments (Chen et al., 2015; Sommer, 1969). A hydraulic fracture is a purely tensile/mode I fracture. However, local shear and antiplane shear fracture modes (II and III) necessarily occur locally at the microscale due to grain-scale heterogeneities and the resulting spatial fluctuation of stresses. The observed cracks overlapping in the micro-CT images in two dimensions (Figure 11) result from local twisting (mode I and mode III failure) formed along the radial parent fracture front. These twisted cracks are part of the secondary cracks forming adjacent to or ahead of the macro/parent fracture, which may include cleavage cracks formed ahead of the fracture front as well. The hydraulic fracturing process is associated with the coalescence of such secondary cracks and the enhancement of the connectivity between fracture segments.

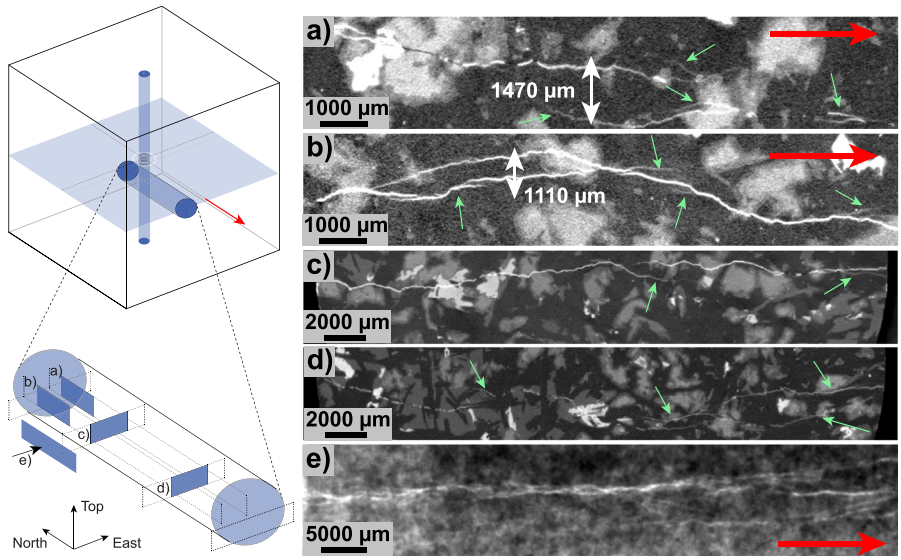

Figure 11. (a–d) Micro-CT images of the fracture paths in GABB-001 (and their location within the overall specimen). The red arrows indicate the fracture propagation direction, while the green arrows indicate the fracture overlapping and bridging with connected areas. (e) The stacked images in the east direction.

The assumption of a single flat hydraulic fracture is no longer valid in the presence of twist fractures/fracture segments. Theoretical studies on a single plane-strain mixed-mode fracture (Lawn, 1993) suggest a decrease in the local energy release rate as the fracture turns into a state of mixed-mode loading. This process is accompanied by an increase of the applied load to maintain the propagation until a new local equilibrium. Likewise, studies on fracture segments (Fleck, 1991; Hattali et al., 2021; Leblond & Frelat, 2014; Leblond et al., 2015) report a decrease of the energy release rate under the same load, which implies a higher energy dissipation for propagation compared to a smooth planar fracture. In the context of a macroradial shape hydraulic fracture consisting of multiple segments, the stress intensity factor is smaller than that of a single flat fracture under uniform pressurization. As a result, a larger fluid pressure and a higher energy input are required to fulfill the propagation criterion. A smaller width is then expected as a result of the elastic interactions of these fracture segments than in a single flat fracture (Germanovich et al., 1997).

One should note that the validity of a uniform pressure distribution in all the segments of the observed fracture must likely be revisited as well. Fluid viscous drop between the segments may likely occur leading to locally elevated pressure promoting link-up. A point that requires further quantification.

The evolution of the fracture segments is closely related to the maximum fracture width, and as such is related to the fluid influx and fracture growth rate. GABB-001 presents the largest stress intensity factor, the slowest propagation velocity, and the largest net pressure at fracture initiation and during the propagation. GABB-003 presents consistent estimates from two different methods in Table 5, indicating a good approximation by elasticity. This probably results from a smaller portion of fracture segments and fracture bridging, which is associated with the largest width (associated with a large influx and fastest growth rate) of GABB-003 among all four experiments. The evolution of the connected areas then correlates with the maximum fracture opening as expected, which is directly related to the fracturing velocity (via the influx rate): the faster grows the fracture, the thicker is the fracture and the fewer bridging areas. Such a correlation may also exist between the bridging areas and the fracture growth regime—when the fracture growth is dominated by fluid viscosity or fluid lag, the fracture width can be larger than that in the toughness dominated regime, thus probably leading to fewer connected areas.

5.3. Comparison With Previous Observations

Fracture segmentation has been reported from laboratory-scale hydraulic fracturing experiments to large-scale hydraulic fractures-dikes in nature.

Fracture segmentation in the laboratory has been reported in brittle materials like PMMA under a mixed-mode loading condition (Wu et al., 2007) and in slit clay (Murdoch, 1993) in absence of such a mixed-mode loading. They observe a plateau of the wellbore injection pressure during the fracture propagation and owe it to the small openings of the point-like connections between the fracture segments, which restricts the fluid flow (Wu et al., 2007). Interestingly, recent studies (Steinhardt & Rubinstein, 2022) have reported another similar fracture morphology for hydraulic fracture growth in PMMA. It appears as long, step-like discontinuities along the fracture surface, which are denoted as step lines. These step lines arise from a local twisting or mixed-mode loading due to material heterogeneity and create additional fracture surfaces leading to an increase in apparent toughness.

Some magmatic dikes have been mapped and shown to be composed of multiple discrete segments arranged in the echelon orientation of dike segments (Delaney & Pollard, 1981; Hoek, 1994). The formation of the segmentation may be attributed to the local rotation of the direction of principal stress. Small offsets of segment contacts, as well as wedge-shaped bodies of crumpled host rock within segments, mark the sites of coalescence of smaller segments during the dike growth (Delaney & Pollard, 1981).

A similar fracture morphology has been observed in industrial hydraulic fracturing treatments (Mahrer, 1999). Fracture offsets due to the crossing of a shear zone or a natural fracture (alternatively called diversion in Rysak et al. (2022)) remain one of the common reasons. Such a morphology imposes local restrictions on the fracture opening and leads to an increase of the real fractured area up to 20% (Rysak et al., 2022). Such an effect may be accumulative in the field with tens of offsets and segments of various sizes and orientations existing along the fracture path. As a result, a significant deviation from the LHFM may be observable characterized by a higher fluid pressure in the wellbore and a slower fracture growth (Jeffrey et al., 2009; Shlyapobersky, 1985; Shlyapobersky et al., 1988).

5.4. Implications for Hydraulic Fracture Mechanics

Although the macroscopic loading associated with a hydraulic fracture is of pure tensile nature, the rock microstructure induces local mode mixity which results in segmentation and bridging. Interestingly, the macroscopic fracture geometry remains planar and circular. For modeling purposes, if the intrinsic length scale of the microstructure is constant, these crack wake effects associated with bridging and segmentation can be lumped into a cohesive zone model—or via a combination of LEFM and cohesive forces to model segments coalescence. This is a typical modeling approach in materials such as rock or alumina-ceramics (Wachtman et al., 2009) for which crack bridging has a first-order impact on the measure of macroscopic fracture energy. The size of the sample in the experiments reported here is clearly on par with the size of the fracture process zone associated with crack bridging. Nevertheless, the data set reported here provides a testing ground for different models associated with crack bridging and segmentation.

In rock masses, at larger scales, larger heterogeneities are likely encountered as the fracture grows in size. This in turn will trigger additional segmentations and bridging at a larger scale. This effect can explain why larger fracture energy spent has been reported for larger fractures/magmatic dikes (see Rivalta et al., 2015 and references therein). Modeling-wise, this effect has been accounted for phenomenologically using the concept of a fracture length-dependent fracture energy (Liu et al., 2019). However, the quantitative connection between the multiscale nature of heterogeneities in rocks and the evolution of such an apparent fracture energy remains to be elucidated.

In a more practical term, the fact that the apparent fracture energy associated with hydraulic fracturing may be larger than the one measured on a small sample reinforces the fact that the maximum recorded pressure (so-called breakdown pressure) should not be used (in combination with a laboratory-derived fracture energy) to estimate the maximum horizontal stress from dual packer microhydraulic fracturing tests, in addition to the problems associated with fluid viscosity effects (Lecampion et al., 2017). However, the relation between closure pressure and minimum stress acting perpendicular remains valid as it is related to the macroscopic geometry of the fracture—with the usual caveats associated with fracture plane reorientation associated with stress field variation around wellbores (Zhang et al., 2011).

6. Conclusions

We have investigated experimentally the growth of hydraulic fractures in Zimbabwe gabbro in the toughness dominated regime, on 25 cm cubic samples under different level of minimum confining stress (from 0 to 10 MPa), keeping the same differential stress (10 MPa). Thanks to an extensive active acoustic array, we are able to properly report important quantities related to the spatiotemporal evolution of these fractures: notably the evolution of the fracture radius from scattered waves, and the fracture width from normally incident transmitted P waves across the fracture. Over the range of minimum confining stress investigated here, no significant effect of confining stress was observed. This is likely due to the low ratio between confining stress and material peak strength (~16 MPa for this gabbro) achieved in these experiments.

Using LEFM and the measured fracture radius (from scattered waves) and fracture width, respectively, we have obtained consistent estimates of the apparent fracture toughness which is larger than the one obtained from semicircular bending tests. Macroscopically, the created fractures are planar and evolve following a mostly radial geometry. However, microscale observations reveal the very important effect of fracture bridging and segmentation associated with local mode mixity triggered by the rock microstructure. The increase of the macroscopically observed energy dissipation can be associated with the overlapping fracture segments and bridging along the fracture path at the lower scale.

At the microscale (here the grain scale), heterogeneities promote shear and antiplane mode fracture conditions locally in addition to the otherwise purely tensile macroscopic loading of hydraulic fracturing. Such local mode mixity promotes fracture segmentation, bridging that coalesces as the fracture size increases. These mechanisms are likely to repeat at larger scales as larger heterogeneities are probed by the propagating fracture, resulting in a further increase of fracture energy.

The use of passive acoustic monitoring in addition to the active acoustic used here should help in further imaging the fracture front propagation. Particularly, the coalescence of fracture segments/breakage of bridges should possibly produce detectable acoustic emission events. In addition, experiments on large specimens with larger confinement although tremendously challenging would be needed to investigate these nonlinear hydraulic fracture mechanics effects under stress conditions similar to the field. This would surely help in further deciphering the scale-dependence of the fracture energy, and guide future theoretical efforts to account for the likely pervasive increase of fracture energy with scales.

Appendix A: Correction Factors for the Finite Sample Dimensions

Y_k and Y_v are correction factors for the stress intensity factor/apparent toughness and the fracture volume accounting for the finite sample dimension of L_b

$$Y_k\left(R/L_b\right) = \left(1 - 0.5R/L_b + 0.148R^3/L_b^3\right) / \left(\sqrt{1 - R/L_b}\right) \tag{A1}$$

$$\begin{aligned} Y_v\left(R/L_b\right) \quad &= \frac{1}{\left(R/L_b\right)^3}\left[1.26\ln\left(\frac{1}{1-\left(R/L_b\right)}\right) - 1.26\left(\frac{R}{L_b}\right) - 0.63\left(\frac{R}{L_b}\right)^2 + 0.58\left(\frac{R}{L_b}\right)^3\right. \\ &\left. -0.315\left(\frac{R}{L_b}\right)^4 - 0.102\left(\frac{R}{L_b}\right)^5 + 0.063\left(\frac{R}{L_b}\right)^6 - 0.0093\left(\frac{R}{L_b}\right)^7 - 0.0081\left(\frac{R}{L_b}\right)^8\right] \end{aligned} \tag{A2}$$

Data Availability Statement

The data set of these experiments is made publicly available at https://doi.org/10.5281/zenodo.3901193 (GABB-001) and https://doi.org/10.5281/zenodo.6610791 (GABB-003, GABB-005, and GABB-006) in the hope of fostering future theoretical and experimental efforts. The source code to reconstruct the fracture geometry is available at https://github.com/GeoEnergyLab-EPFL/FracMonitoring.git.

Acknowledgments
This work was funded by the Swiss National Science Foundation under Grant 200021-192237. The authors would like to thank Professors Petro Reis, Marie Violay, and Lyesse Laloui for access to their experimental equipment to measure surface roughness and material properties. The authors thank Antonio Salazar Vásquez for testing the static elastic properties of gabbro, and Karan Mittal for performing part of the semicircular bending tests. The help of Gary Perrenoud, Michael Monnet, Jeremie Bettex, and Swan Brede in performing hydraulic fracturing experiments are gratefully acknowledged.

References

Aben, F. M., Brantut, N., Mitchell, T. M., & David, E. C. (2019). Rupture energetics in crustal rock from laboratory-scale seismic tomography. *Geophysical Research Letters*, *46*, 7337–7344. https://doi.org/10.1029/2019GL083040

Anderson, T. L. (2017). *Fracture mechanics: Fundamentals and applications*. CRC Press.

Bahat, D. (1991). *Tectonofractography*. Springer.

Bao, G., & Suo, Z. (1992). Remarks on crack-bridging concepts. *Applied Mechanics Reviews*, *45*(8), 355–366. https://doi.org/10.1115/1.3119764

Bažant, Z. P. (1984). Size effect in blunt fracture: Concrete, rock, metal. *Journal of Engineering Mechanics*, *110*(4), 518–535.

Bazant, Z. P., & Planas, J. (1998). *Fracture and size effect in concrete and other quasibrittle materials* (Vol. 16). CRC Press.

Bunger, A. P. (2006). A photometry method for measuring the opening of fluid-filled fractures. *Measurement Science and Technology*, *17*(12), 3237–3244. https://doi.org/10.1088/0957-0233/17/12/006

Bunger, A. P., & Detournay, E. (2008). Experimental validation of the tip asymptotics for a fluid-driven crack. *Journal of the Mechanics and Physics of Solids*, *56*(11), 3101–3115. https://doi.org/10.1016/j.jmps.2008.08.006

Bunger, A. P., Jeffrey, R. G., & Detournay, E. (2005). Application of scaling laws to laboratory-scale hydraulic fractures. In *Alaska Rocks 2005, the 40th US Symposium on Rock Mechanics (USRMS)* (p. ARMA/USRMS-05-818). Anchorage, AK.

Chen, C. H., Cambonie, T., Lazarus, V., Nicoli, M., Pons, A. J., & Karma, A. (2015a). Crack front segmentation and facet coarsening in mixed-mode fracture. *Physical Review Letters*, *115*(26), 265503. https://doi.org/10.1103/physrevlett.115.265503

Chen, Y., Nagaya, Y., & Ishida, T. (2015b). Observations of fractures induced by hydraulic fracturing in anisotropic granite. *Rock Mechanics and Rock Engineering*, *48*(4), 1455–1461. https://doi.org/10.1007/s00603-015-0727-9

Delaney, P. T., & Pollard, D. D. (1981). *Deformation of host rocks and flow of magma during growth of minette dikes and breccia-bearing intrusions near Ship Rock, New Mexico* (Tech. Rep.). Washington, DC: U.S. Geological Survey.

Detournay, E. (2016). Mechanics of hydraulic fractures. *Annual Review of Fluid Mechanics*, *48*, 311–339. https://doi.org/10.1146/annurev-fluid-010814-014736

Fleck, N. A. (1991). Brittle fracture due to an array of microcracks. *Proceedings of the Royal Society of London. Series A: Mathematical and Physical Sciences*, *432*(1884), 55–76.

Garagash, D. I. (2009). *Scaling of physical processes in fluid-driven fracture: Perspective from the tip*. In IUTAM Symposium on Scaling in Solid Mechanics (pp. 91–100). https://doi.org/10.1007/978-1-4020-9033-2_9

Garagash, D. I. (2019). Cohesive-zone effects in hydraulic fracture propagation. *Journal of the Mechanics and Physics of Solids*, *133*, 103727. https://doi.org/10.1016/j.jmps.2019.103727

Germanovich, L. N., Ring, L. M., Astakhov, D. K., Shlyapobersky, J., & Mayerhofer, M. J. (1997). Hydraulic fracture with multiple segments II. Modeling. *International Journal of Rock Mechanics and Mining Sciences*, *34*(3–4), 98.e1–98.e15. https://doi.org/10.1016/s1365-1609(97)00079-8

Groenenboom, J., & Fokkema, J. T. (1998). Monitoring the width of hydraulic fractures with acoustic waves. *Geophysics*, *63*(1), 139–148. https://doi.org/10.1190/1.1444306

Groenenboom, J., & van Dam, D. B. (2000). Monitoring hydraulic fracture growth: Laboratory experiments. *Geophysics*, *65*(2), 603–611. https://doi.org/10.1190/1.1444756

Haas, A., Revil, A., Karaoulis, M., Frash, L., Hampton, J., Gutierrez, M., & Mooney, M. (2013). Electric potential source localization reveals a borehole leak during hydraulic fracturing. *Geophysics*, *78*(2), D93–D113. https://doi.org/10.1190/geo2012-0388.1

Haimson, B. (1968). *Hydraulic fracturing in porous and nonporous rock and its potential for determining in-situ stresses at great depth*. University of Minnesota.

Hattali, M., Cambonie, T., & Lazarus, V. (2021). Toughening induced by the formation of facets in mode I + III brittle fracture: Experiments versus a two-scale cohesive zone model. *Journal of the Mechanics and Physics of Solids*, *156*, 104596. https://doi.org/10.1016/j.jmps.2021.104596

Hoek, J. D. (1994). *Mafic dykes of the vestfold hills, east Antarctica. an analysis of the emplacement mechanism of tholeiitic dyke swarms and of the role of dyke emplacement during crustal extension (Doctoral dissertation)*. Utrecht, Netherlands: Utrecht University. Retrieved from https://dspace.library.uu.nl/handle/1874/295361

Hubbert, M. K., & Willis, D. G. (1957). Mechanics of hydraulic fracturing. *Transactions of the AIME*, *210*, 153–168. https://doi.org/10.2118/686-g

Irwin, G. R. (1957). Analysis of stresses and strains near the end of a crack traversing a plate. *Journal of Applied Mechanics*, *24*, 361–364. https://doi.org/10.1115/1.4011547

Jeffrey, R. G., Bunger, A., Lecampion, B., Zhang, X., Chen, Z., van As, A., et al. (2009). Measuring hydraulic fracture growth in naturally fractured rock. In *SPE Annual Technical Conference and Exhibition*.

Kinloch, A., & Williams, J. (1980). Crack blunting mechanisms in polymers. *Journal of Materials Science*, *15*(4), 987–996. https://doi.org/10.1007/bf00552112

Kovalyshen, Y., Bunger, A. P., Kear, J., & Kasperczyk, D. (2014). Comparison between ultrasonic and photometric methods for hydraulic fracture laboratory monitoring. *International Journal of Rock Mechanics and Mining Sciences*, *70*, 368–374. https://doi.org/10.1016/j.ijrmms.2014.05.008

Kuruppu, M., Obara, Y., Ayatollahi, M., Chong, K., & Funatsu, T. (2014). ISRM-suggested method for determining the mode I static fracture toughness using semi-circular bend specimen. *Rock Mechanics and Rock Engineering*, *47*(1), 267–274. https://doi.org/10.1007/s00603-013-0422-7

Labuz, J., Shah, S., & Dowding, C. (1987). The fracture process zone in granite: Evidence and effect. *International Journal of Rock Mechanics and Mining Sciences & Geomechanics Abstracts*, *24*, 235–246. https://doi.org/10.1016/0148-9062(87)90178-1

Lama, R., & Vutukuri, V. (1978). Handbook on mechanical properties of rocks-testing techniques and results-volume III (Vol. *3*(2)).

Lawn, B. R. (1993). *Fracture of brittle solids*. Cambridge University Press.

Leblond, J.-B., & Frelat, J. (2014). Development of fracture facets from a crack loaded in mode I + III: Solution and application of a model 2D problem. *Journal of the Mechanics and Physics of Solids*, *64*, 133–153. https://doi.org/10.1016/j.jmps.2013.11.001

Leblond, J.-B., Lazarus, V., & Karma, A. (2015). Multiscale cohesive zone model for propagation of segmented crack fronts in mode I + III fracture. *International Journal of Fracture*, *191*(1), 167–189. https://doi.org/10.1007/s10704-015-0001-x

Lecampion, B., Desroches, J., Jeffrey, R. G., & Bunger, A. P. (2017). Experiments versus theory for the initiation and propagation of radial hydraulic fractures in low permeability materials. *Journal of Geophysical Research: Solid Earth*, *122*, 1239–1263. https://doi.org/10.1002/2016JB013183

Lhomme, T. P. Y. (2005). *Initiation of hydraulic fractures in natural sandstones*. TU Delft, Delft University of Technology.

Liu, D. (2021). *Hydraulic fracture growth in quasi-brittle materials (Doctoral dissertation)*. Lausanne, Switzerland: EPFL. https://doi.org/10.5075/epfl-thesis-8360

Liu, D., & Lecampion, B. (2019a). Growth of a radial hydraulic fracture accounting for the viscous fluid flow in a rough cohesive zone. In *ARMA-CUPB Geothermal International Conference*.

Liu, D., & Lecampion, B. (2019b). Propagation of a plane-strain hydraulic fracture accounting for the presence of a cohesive zone and a fluid lag. In *53rd US Rock Mechanics/Geomechanics Symposium*.

Liu, D., & Lecampion, B. (2021). Propagation of a plane-strain hydraulic fracture accounting for a rough cohesive zone. *Journal of the Mechanics and Physics of Solids*, *149*, 104322. https://doi.org/10.1016/j.jmps.2021.104322

Liu, D., & Lecampion, B. (To appear). Measurements of the evolution of the fluid lag in laboratory hydraulic fracture experiments in rocks. In Mechanics of hydraulic fracturing. Wiley.

Liu, D., Lecampion, B., & Blum, T. (2020). Time-lapse reconstruction of the fracture front from diffracted waves arrivals in laboratory hydraulic fracture experiments. *Geophysical Journal International*, *223*(1), 180–196. https://doi.org/10.1093/gji/ggaa310

Liu, D., Lecampion, B., & Garagash, D. I. (2019). Propagation of a fluid-driven fracture with fracture length dependent apparent toughness. *Engineering Fracture Mechanics*, *220*, 106616. https://doi.org/10.1016/j.engfracmech.2019.106616

Lockner, D., & Byerlee, J. D. (1977). Hydrofracture in weber sandstone at high confining pressure and differential stress. *Journal of Geophysical Research*, *82*(14), 2018–2026. https://doi.org/10.1029/JB082i014p02018

Mahrer, K. D. (1999). A review and perspective on far-field hydraulic fracture geometry studies. *Journal of Petroleum Science and Engineering*, *24*(1), 13–28. https://doi.org/10.1016/s0920-4105(99)00020-0

Makhnenko, R. Y., Bunger, A. P., & Detournay, E. (2010). Deviation from linear elastic fracture in near-surface hydraulic fracturing experiments with rock. In *44th US Rock Mechanics Symposium and 5th US-Canada Rock Mechanics Symposium*.

Medlin, W., & Masse, L. (1984). Laboratory experiments in fracture propagation. *Society of Petroleum Engineers Journal*, *24*(03), 256–268. https://doi.org/10.2118/10377-pa

Moore, J. R., & Glaser, S. D. (2007). Self-potential observations during hydraulic fracturing. *Journal of Geophysical Research*, *112*, B02204. https://doi.org/10.1029/2006JB004373

Moukhtari, F.-E. (2020). *Propagation of fluid driven fractures in transversely isotropic material (Doctoral dissertation)*. Lausanne, Switzerland: EPFL. https://doi.org/10.5075/epfl-thesis-7470

Murdoch, L. C. (1993). Hydraulic fracturing of soil during laboratory experiments. Part 1. Methods and observations. *Géotechnique*, *43*(2), 255–265. https://doi.org/10.1680/geot.1993.43.2.255

Papanastasiou, P. (1999). The effective fracture toughness in hydraulic fracturing. *International Journal of Fracture*, *96*(2), 127–147. https://doi.org/10.1023/a:1018676212444

Renard, F., Bernard, D., Desrues, J., & Ougier-Simonin, A. (2009). 3D imaging of fracture propagation using synchrotron X-ray microtomography. *Earth and Planetary Science Letters*, *286*(1–2), 285–291. https://doi.org/10.1016/j.epsl.2009.06.040

Ricker, N. (1951). The form and laws of propagation of seismic wavelets. In *3rd World Petroleum Congress*.

Ritchie, R. O. (2011). The conflicts between strength and toughness. *Nature Materials*, *10*(11), 817–822. https://doi.org/10.1038/nmat3115

Rivalta, E., Taisne, B., Bunger, A. P., & Katz, R. F. (2015). A review of mechanical models of dike propagation: Schools of thought, results and future directions. *Tectonophysics*, *638*, 1–42. https://doi.org/10.1016/j.tecto.2014.10.003

Roshankhah, S., Marshall, J., Tengattini, A., Ando, E., Rubino, V., Rosakis, A., et al. (2018). Neutron imaging: A new possibility for laboratory observation of hydraulic fractures in shale? *Géotechnique Letters*, *8*(4), 316–323. https://doi.org/10.1680/jgele.18.00129

Rummel, F. (1987). Fracture mechanics approach to hydraulic fracturing stress measurements. *Fracture Mechanics of Rock*, 217–240. https://doi.org/10.1016/b978-0-12-066266-1.50011-9

Rysak, B., Gale, J. F., Laubach, S. E., & Ferrill, D. A. (2022). Mechanisms for the generation of complex fracture networks: Observations from slant core, analog models, and outcrop. *Frontiers of Earth Science*, *10*, 848012. https://doi.org/10.3389/feart.2022.848012

Savitski, A., & Detournay, E. (2002). Propagation of a penny-shaped fluid-driven fracture in an impermeable rock: Asymptotic solutions. *International Journal of Solids and Structures*, *39*(26), 6311–6337. https://doi.org/10.1016/s0020-7683(02)00492-4

Shlyapobersky, J. (1985). Energy analysis of hydraulic fracturing. In *The 26th US Symposium on Rock Mechanics (USRMS)*.

Shlyapobersky, J., Wong, G., & Walhaug, W. (1988). Overpressure calibrated design of hydraulic fracture stimulations. In *SPE Annual Technical Conference and Exhibition*.

Sneddon, I. N. (1946). The distribution of stress in the neighbourhood of a crack in an elastic solid. *Proceedings of the Royal Society of London. Series A*, *187*(1009), 229–260.

Sommer, E. (1969). Formation of fracture 'lances' in glass. *Engineering Fracture Mechanics*, *1*(3), 539–546. https://doi.org/10.1016/0013-7944(69)90010-1

Stanchits, S., Surdi, A., Gathogo, P., Edelman, E., & Suarez-Rivera, R. (2014). Onset of hydraulic fracture initiation monitored by acoustic emission and volumetric deformation measurements. *Rock Mechanics and Rock Engineering*, *47*(5), 1521–1532. https://doi.org/10.1007/s00603-014-0584-y

Steinhardt, W., & Rubinstein, S. M. (2022). How material heterogeneity creates rough fractures. *Physical Review Letters*, *129*(12), 128001. https://doi.org/10.1103/physrevlett.129.128001

Stoeckhert, F., Molenda, M., Brenne, S., & Alber, M. (2015). Fracture propagation in sandstone and slate-laboratory experiments, acoustic emissions and fracture mechanics. *Journal of Rock Mechanics and Geotechnical Engineering*, *7*(3), 237–249. https://doi.org/10.1016/j.jrmge.2015.03.011

Tada, H., Paris, P. C., & Irwin, G. R. (1973). *The stress analysis of cracks*. Hellertown, PA: Del Research Corp.

Tarantola, A. (2005). *Inverse problem theory and methods for model parameter estimation*. SIAM.

Thallak, S., Holder, J., & Gray, K. (1993). The pressure dependence of apparent hydrofracture toughness. In *The 34th US Symposium on Rock Mechanics (USRMS)*. Madison, WI.

Tvergaard, V., & Hutchinson, J. W. (1992). The relation between crack growth resistance and fracture process parameters in elastic-plastic solids. *Journal of the Mechanics and Physics of Solids*, *40*(6), 1377–1397. https://doi.org/10.1016/0022-5096(92)90020-3

van Dam, D. B., & de Pater, C. J. (1999). Roughness of hydraulic fractures: The importance of in-situ stress and tip processes. In *SPE Annual Technical Conference and Exhibition*.

Vásquez, A. S., Rabaiotti, C., Germanovich, L. N., & Puzrin, A. M. (2022). Distributed fiber optics measurements of rock deformation and failure in triaxial tests. *Journal of Geophysical Research: Solid Earth*, *127*, e2022JB023997. https://doi.org/10.1029/2022JB023997

Wachtman, J. B., Cannon, W. R., & Matthewson, M. J. (2009). *Mechanical properties of ceramics*. John Wiley & Sons.

Warpinski, N. (1985). Measurement of width and pressure in a propagating hydraulic fracture. *Society of Petroleum Engineers Journal*, *25*(01), 46–54. https://doi.org/10.2118/11648-pa

Wu, R., Bunger, A. P., Jeffrey, R. G., & Siebrits, E. (2008). A comparison of numerical and experimental results of hydraulic fracture growth into a zone of lower confining stress. In *The 42nd US Rock Mechanics Symposium (USRMS)*.

Wu, R., Germanovich, L. N., Van Dyke, P. E., & Lowell, R. P. (2007). Thermal technique for controlling hydraulic fractures. *Journal of Geophysical Research*, *112*, B05209. https://doi.org/10.1029/2005JB003815

Xing, P., Bunger, A. P., Yoshioka, K., Adachi, J., & El-Fayoumi, A. (2016). Experimental study of hydraulic fracture containment in layered reservoirs. In *50th US Rock Mechanics/Geomechanics Symposium*.

Zhang, Z., Jeffrey, R. G., Bunger, A. P., & Thiercelin, M. (2011). Initiation and growth of a hydraulic fracture from a circular wellbore. *International Journal of Rock Mechanics and Mining Sciences*, *48*, 984–995. https://doi.org/10.1016/j.ijrmms.2011.06.005

Zoback, M., Rummel, F., Jung, R., & Raleigh, C. (1977). Laboratory hydraulic fracturing experiments in intact and pre-fractured rock. *International Journal of Rock Mechanics and Mining Sciences & Geomechanics Abstracts*, *14*, 49–58. https://doi.org/10.1016/0148-9062(77)90196-6